Article

Cell Reports

Division and Adaptation to Host Environment of Apicomplexan Parasites Depend on Apicoplast Lipid Metabolic Plasticity and Host Organelle Remodeling

Graphical Abstract

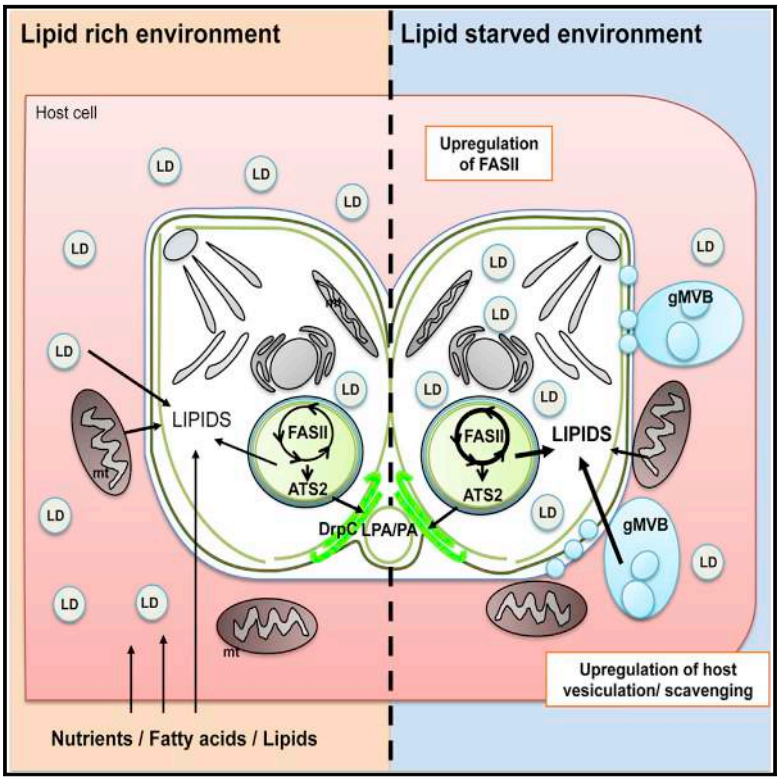

Highlights

- Knockout of apicoplast *Tg*ATS2 disrupts LPA/PA for DrpC recruitment during cytokinesis
- *T. gondii* can sense host environment and adapt to low host nutritional content
- Under lipid starvation, parasite FASII and other lipid metabolic genes become essential
- Upon nutrient deprivation, *T. gondii* induces host organelle remodeling and vesiculation

Authors

Souad Amiar, Nicholas J. Katris, Laurence Berry, ..., Geoffrey I. McFadden, Yoshiki Yamaryo-Botté, Cyrille Y. Botté

Correspondence

yoshiki.yamaryo@gmail.com (Y.Y.-B.), cyrille.botte@univ-grenoble-alpes.fr (C.Y.B.)

In Brief

Apicoplast *de novo* lipid synthesis and lipid host scavenging are both critical for apicomplexan intracellular development. Amiar et al. show that the parasite adapts to the fluctuations of host nutritional content to regulate the metabolic activity of both apicoplast and scavenging pathways and maintain parasite development and division.

Amiar et al., 2020, Cell Reports *30*, 3778–3792
March 17, 2020
https://doi.org/10.1016/j.celrep.2020.02.072

CellPress

OPEN ACCESS
CellPress

Cell Reports
Article

Division and Adaptation to Host Environment of Apicomplexan Parasites Depend on Apicoplast Lipid Metabolic Plasticity and Host Organelle Remodeling

Souad Amiar,[1,5] Nicholas J. Katris,[1,5] Laurence Berry,[2] Sheena Dass,[1] Samuel Duley,[1] Christophe-Sebastien Arnold,[1] Melanie J. Shears,[3] Camille Brunet,[1] Bastien Touquet,[4] Geoffrey I. McFadden,[3] Yoshiki Yamaryo-Botté,[1,6,*] and Cyrille Y. Botté[1,6,7,*]

[1]ApicoLipid Team, Institute for Advanced Biosciences, CNRS UMR5309, Université Grenoble Alpes, INSERM U1209, Grenoble, France
[2]Dynamique des interactions Membranaires normales et pathologiques, UMR5235, Université Montpellier II, Montpellier, France
[3]McFadden Laboratory, School of Biosciences, University of Melbourne, Melbourne, VIC 3010, Australia
[4]Team Cell and Membrane Dynamics of Parasite-Host Interaction, Institute for Advanced Biosciences, INSERM 1209, CNRS UMR5309, Université Grenoble Alpes, Grenoble, France
[5]These authors contributed equally
[6]Senior author
[7]Lead Contact
*Correspondence: yoshiki.yamaryo@gmail.com (Y.Y.-B.), cyrille.botte@univ-grenoble-alpes.fr (C.Y.B.)
https://doi.org/10.1016/j.celrep.2020.02.072

SUMMARY

Apicomplexan parasites are unicellular eukaryotic pathogens that must obtain and combine lipids from both host cell scavenging and *de novo* synthesis to maintain parasite propagation and survival within their human host. Major questions on the role and regulation of each lipid source upon fluctuating host nutritional conditions remain unanswered. Characterization of an apicoplast acyltransferase, *Tg*ATS2, shows that the apicoplast provides (lyso) phosphatidic acid, required for the recruitment of a critical dynamin (*Tg*DrpC) during parasite cytokinesis. Disruption of *Tg*ATS2 also leads parasites to shift metabolic lipid acquisition from *de novo* synthesis toward host scavenging. We show that both lipid scavenging and *de novo* synthesis pathways in wild-type parasites exhibit major metabolic and cellular plasticity upon sensing host lipid-deprived environments through concomitant (1) upregulation of *de novo* fatty acid synthesis capacities in the apicoplast and (2) parasite-driven host remodeling to generate multi-membrane-bound structures from host organelles that are imported toward the parasite.

INTRODUCTION

Apicomplexa are intracellular protozoan parasites that cause serious infectious diseases in humans, including malaria and toxoplasmosis. Most Apicomplexa harbor a relict non-photosynthetic plastid, the apicoplast, acquired by the secondary endosymbiosis of a red alga (Janouskovec et al., 2010). The apicoplast lost photosynthetic capability during the conversion to a parasitic lifestyle (Botté et al., 2013). However, it still contains plant-like pathways, including a prokaryotic type II fatty acid synthesis pathway (FASII) (Waller et al., 1998). The apicoplast is essential for parasite survival in both *T. gondii* and *P. falciparum* (MacRae et al., 2012).

However, the FASII pathway is thought to be essential only during specific life stages. Indeed, in *Plasmodium*, disruption of FASII was demonstrated to be dispensable in asexual blood stages but essential for late liver stage in rodent malaria parasites and for sporozoite schizogony during mosquito stages (Vaughan et al., 2009). Nevertheless, changes in *P. falciparum* blood stage growth conditions, such as lipid starvation during *in vitro* growth and physiological stress in human patients, induced re-activation of apicoplast FASII (Daily et al., 2007; Botté et al., 2013), suggesting plasticity of FASII in response to nutritional environment. In *T. gondii*, FASII is essential during tachyzoite development (Mazumdar et al., 2006).

Apicomplexan parasite membranes are constituted of up to 80% phospholipid (PL), primarily phosphatidylcholine (PC), phosphatidylethanolamine (PE), phosphatidylserine (PS), and phosphatidylinositol (PI; Welti et al., 2007; Gulati et al., 2015). *T. gondii* can readily scavenge PL and triacylglycerols (TAGs) from the host but is also capable of, and dependent on, *de novo* synthesis of several PL classes (Hu et al., 2017; Amiar et al., 2016; Nolan et al., 2017). Like other eukaryotes, apicomplexan *de novo* PL synthesis is initiated by the assembly of fatty acid (FA) (i.e., esterification onto a glycerol-phosphate backbone) into specific PL precursors. In *T. gondii*, FAs to be used for PLs synthesis derive from three sources: (1) apicoplast FASII generating short FA chains (C12:0, C14:0, and C16:0) (Ramakrishnan et al., 2012), (2) FA elongases located on the parasite endoplasmic reticulum (ER) generating C16:1, C18:1, C20:1, C22:1, and C26:1 (Dubois et al., 2018), and (3) FAs directly scavenged from the host cell (Bisanz et al., 2006). Lipidomics reveals that most *T. gondii* PLs are hybrid/patchwork molecules, comprising one FA moiety from the apicoplast *de novo* synthesis pathway and a second one scavenged from the host (Amiar et al., 2016). Thus, both scavenging and *de novo* synthesis of FA are critical for intracellular development.

Typically, phosphatidic acid (PA) is the central precursor for the *de novo* synthesis of all PL classes by the two-step esterification of FAs onto a glycerol-3-phosphate backbone; first by glycerol-3-phosphate acyltransferases (GPATs) to form lysophosphatidic acid (LPA) and then by acyl-glycerol-3-phosphate acyltransferases (AGPATs) to convert LPA to PA. In eukaryotic cells, GPATs and AGPATs of diverse origins work as a set at several locations within the cell. Apicomplexans have two sets of acyltransferases: one plastid-like set putatively in the apicoplast (prokaryotic pathway) (Amiar et al., 2016) and another pair predicted to be in the ER (the so-called eukaryotic pathway). In *T. gondii*, the apicoplast GPAT, *Tg*ATS1 is essential for tachyzoite development, where it generates LPA from apicoplast-FA for the bulk synthesis of PL (Amiar et al., 2016). The role of parasite AGPATs for lipid synthesis is yet to be determined. Beyond their roles as lipid precursors, PA (and LPA) also have important biophysical properties by controlling the formation of positive or negative membrane curvatures, and thereby influence the recruitment of proteins involved in membrane fusion/fission events such as endocytosis in other eukaryotic models (Schmidt et al., 1999; Kooijman et al., 2005; Brown et al., 2008).

Here we characterize *T. gondii* AGPATs, focusing on one localized to the apicoplast, *Tg*ATS2. We confirm that *Tg*ATS2 is an acyltransferase by heterologous complemention of a bacterial mutant. We then generate a knockout (KO) mutant, which was defective parasite cytokinesis and normal lipid profile. Particularly, the impact of LPA/PA changes on the localization of a dynamin-related protein (Drp), *Tg*DrpC, in the *Tg*ATS2 mutant is described and provides a rationale for cytokinesis defects associated with drug inhibition of apicoplast FASII (Martins-Duarte et al., 2015). Finally, changes in parasite lipid composition and lipid fluxes led us to subject parasites to lipid starvation to explore how host nutritional environment affects parasite growth. Analysis of lipid fluxes and growth screening under adverse lipid conditions show that parasites can sense the environment and respond by (1) upregulation of *de novo* lipid synthesis in the apicoplast and (2) manipulation of the human host through vesiculation from host organelles and import of such material to the parasitophorous vacuole (PVM) mediated by export of parasite effectors to improve their lipid scavenging. Our analysis provides unprecedented mechanistic insights into parasite metabolic adaption under host nutritional challenge, which was poorly understood until now.

RESULTS

Deletion of *Toxoplasma gondii* Apicoplast Acyltransferase *Tg*ATS2 Results in Aberrant Cytokinesis and Residual Body Formation during Replication

To explore *de novo* PA synthesis in *T. gondii*, we searched the genome for AGPATs capable of catalyzing the esterification of an activated FA (i.e., acyl-CoA or acyl-ACP) onto LPA to make PA. We found two AGPAT candidates with conserved motifs: ToxoDB: TGME49_297640 and ToxoDB: TGME49_240860. Phylogenetic analyses reveal that TGME49_297640 clusters with the prokaryotic clade of the pathway with plant and algal sequences and that TGME49_240860 clusters with the eukaryotic clade of the pathway (Figure S1). We termed these enzymes *Tg*ATS2 and *Tg*AGPAT on the basis of the plant and eukaryotic terminology, respectively. We generated parasite lines expressing *Tg*ATS2 and *Tg*AGPAT endogenously tagged at the C terminus with a triple HA tag, under control of their respective promoters (Figures S2A–S2C). Immunofluorescence assays (IFAs) confirmed *Tg*ATS2 targets to the apicoplast (Figure 1A), and transient expression of *Tg*AGPAT-HA showed a perinuclear structure corresponding to the parasite ER (Figure 1B).

To test if *Tg*ATS2 and *Tg*AGPAT are functional AGPAT, we complemented an *E. coli* temperature-sensitive mutant SM2-1 Δ*plsC* lacking AGPAT activity (Coleman, 1990) with recombinant *TgATS2* and *TgAGPAT*. All transformants grew at the permissive temperature of 30°C (Figure 1C). Only those complemented with bacterial *Ec*PlsC and *Tg*ATS2 grew at the non-permissive 42°C (Figure 1C). Constructs with *TgAGPAT* including or not its long N-Ter extension did not grow at 42°C, likely because of *TgAGPAT* eukaryotic origin (Figure S1). Indeed, eukaryotic AGPATs favor acyl-CoA substrates over acyl-ACP substrates used in bacterial and plastid systems. Thus, it is unclear if *Tg*AGPAT has acyltransferase activity, but *Tg*ATS2 complements defective *E. coli* SM2-1 AGPAT enzymatic activity *in vivo*, confirming LPA-to-PA synthetic capability.

To investigate the importance of apicoplast *Tg*ATS2 during tachyzoite life stages, the *TgATS2* locus was disrupted to generate knock-in (KI) and KO mutants of *Tg*ATS2 using CRISPR-Cas9 strategies (Figures S2D–S2F). Loss of the protein product was confirmed by western blot (Figures 1D and 1E), IFA (Figure 1F), and PCR (Figures S2E and S2F). Both Δ*Tg*ATS2 mutants were viable, but plaque and replication assays revealed that Δ*Tg*ATS2 had a mild yet significant growth defect with significantly more small (two to four parasites) vacuoles and significantly fewer large vacuoles (Figures 1G–1I).

Parasite egress was significantly affected in the Δ*Tg*ATS2 mutant (Figure S2G), but invasion ability showed no difference with the parental line, nor was there a defect in microneme secretion (Figures S2H and S2I). Morphology of different intracellular tachyzoite organelles showed no obvious defects except the apicoplast displaying a mild biogenesis defect (Figures S2J and S2K).

Upon closer inspection of parasite morphology, Δ*Tg*ATS2 parasites appeared fused to each other at their basal poles (Figure 2A), suggesting a cytokinesis defect, which provided a rationale for the egress defect (Figure S2G). Cytokinesis was monitored by localizing MORN1, which curiously displayed no obvious basal mis-localization (Figure 2B). However, Δ*Tg*ATS2 parasites showed important enlargement of the residual body (Figure 2C). Residual body size was quantified by IFA using GAP45 antibody as a marker for the inner membrane complex (IMC). Δ*Tg*ATS2 parasites displayed a significantly larger residual body at the center of big vacuoles (more than four parasites), (Figures 2B and 2C). Accordingly, egressed extracellular parasites often remained tethered at their basal pole via a plasma membrane (PM) structure (Figure 2D). Electron microscopy (EM) of Δ*Tg*ATS2 parasites supported the segregation defects seen by IFA (Figure 2E). In dividing parasites, it is commonly seen that the PM is kept connected between two recently divided cells so that the cells are stuck together and distributed

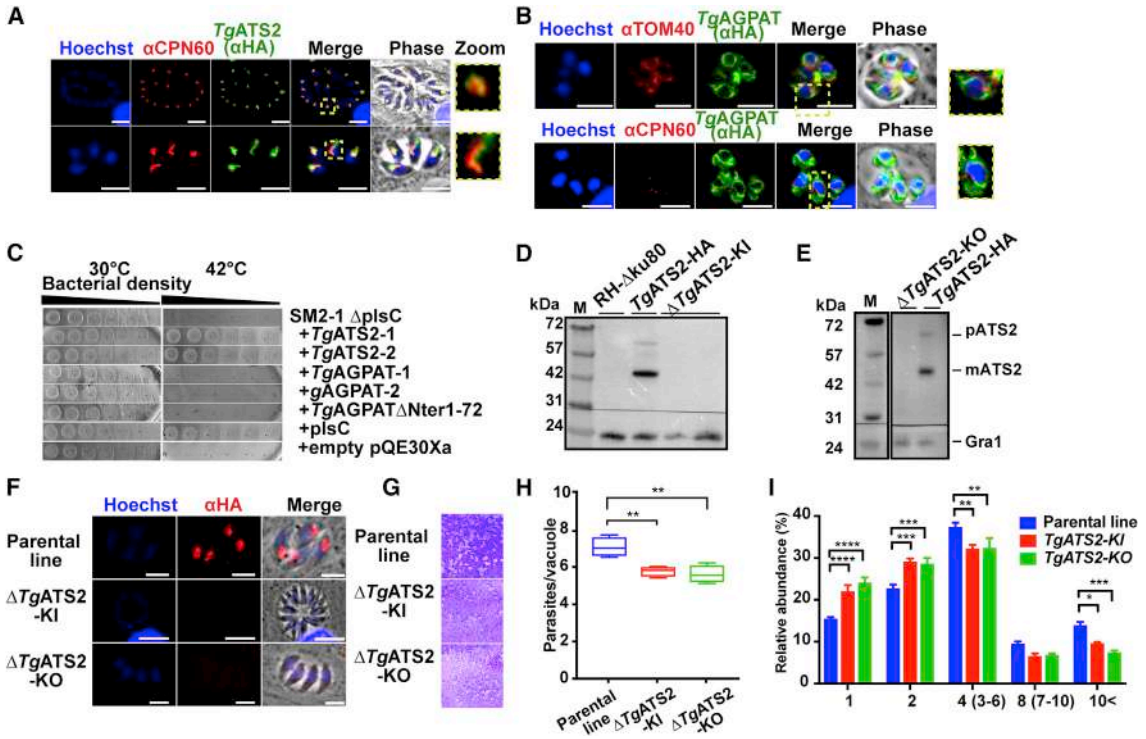

Figure 1. *Tg*ATS2 Is an Apicoplast Lysophosphatidic Acid Acyltransferase Important for Parasite Proliferation

(A and B) IFA of stable *Tg*ATS2-HA expressing parasites (A) and transient *Tg*AGPAT-HA expression (B). CPN60, apicoplast marker; TOM40, mitochondrial marker. Scale bars, 2 μm.

(C) Expression of *Tg*ATS2 and *Tg*AGPAT in LPAAT-deficient *E. coli* strain SM2-1. SM2-1Δ*plsC E. coli* mutant transformed with *Tg*ATS2 (1, 2), *Tg*AGPAT (1, 2), $TgAGPAT_{\Delta Nter1\text{-}72}$, *Ec*plsC, or empty pQE30Xa expression vector were grown at 30°C (permissive) or 42°C (non-permissive) for 20 h (n = 3).

(D and E) Confirmation of *Tg*ATS2-HA loss by western blot analysis in *Tg*ATS2-KI (D) and *Tg*ATS2-KO (E) using anti-HA (anti-Gra1, loading control).

(F) Confirmation of *Tg*ATS2-HA signal loss in Δ*Tg*ATS2 by IFA using anti-HA. Scale bars, 2 μm.

(G) Plaque assay showing a mild growth defect in Δ*Tg*ATS2 mutants.

(H) Cell-based growth fitness assay confirmed the growth defect in the Δ*Tg*ATS2 mutants 30 h post-infection (n = 3).

(I) Proliferation assay confirmed a replication defect in Δ*Tg*ATS2 mutants (n = 3).

*p ≤ 0.05, **p ≤ 0.01, ***p ≤ 0.001, and ****p ≤ 0.0001.

to daughter cells during cytokinesis. Very little is known on the molecular mechanisms of PM segregation during cytokinesis. In the parental parasites, initial steps of endodyogeny showed the formation of the daughter cell apical pole along with organelle division before the formation of the daughter cells within the mother cell (Figure 2E). Emergence of the daughter cells initiates the apical-to-basal biogenesis of their PM, partly recycled from the mother (Figures 2E1–2E5), and ends by a constriction of both IMC and PM at the basal poles, leaving a small basal residual body (Figure 2E6). In contrast, there were many division and cytokinesis defects in Δ*Tg*ATS2, which were unable to separate, although a new round of daughter formation could be initiated (Figure 2E1). Furthermore, parasite organelles were frequently found in the residual body as if ejected from improper segregation, likely contributing to the enlarged residual body phenotype (Figure 2E). Affected vacuoles thus displayed enlarged residual bodies that often contained various organelles—including the nucleus, mitochondrion, acidocalcisome vesicles, and other cytosolic material—that appeared to be ejected from the dividing cells because of improper segregation (Figures 2E3 and 2E4). Pieces of mitochondria were a particular feature within enlarged residual bodies (Figures 2E5 and 2E6).

We attempted to disrupt *TgAGPAT* using CRISPR-Cas9 as per Δ*Tg*ATS2 in wild-type (WT) (Δ*Tg*AGPAT) and Δ*TgATS2* (Δ*Tg*AGPAT-Δ*Tg*ATS2) genetic backgrounds, but parasites were not viable (Figures S2L–S2O), suggesting that *Tg*AGPAT is indispensable, consistent with its phenotype score (Sidik et al., 2016).

*Tg*ATS2 Disruption Reduces C14:0 FA Incorporation into *T. gondii* Lipids, Skews the LPA/PA Ratio, and Alters PL Abundance and Composition

To investigate the role of *Tg*ATS2 in lipid metabolism, we performed lipidomic analysis on the Δ*Tg*ATS2 mutant. Disruption of *Tg*ATS2 resulted in a large significant reduction of the relative amount of C14:0, the main product of the apicoplast FASII (Figures 3A and 3B). Significant decreases in C18:1 and C20:1 were also observed (Figures 3A and 3B). In contrast, there were significant increases in the abundance of C18:0, C22:1, C24:1, C20:4, C20:5, and C22:6 (Figures 3A–3C), most of which can be

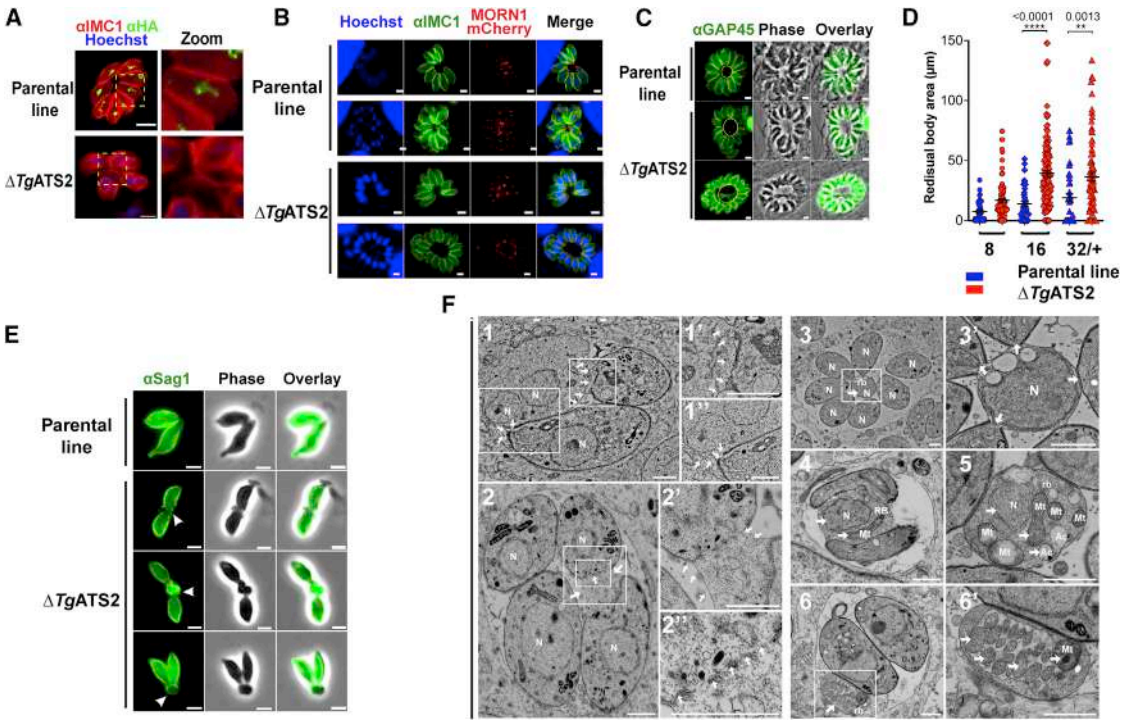

Figure 2. Disruption of *Tg*ATS2 Induces Parasite Cytokinetic Defect, Residual Body Enlargement, and Organelle Segregation Deficiency

(A) IFA of Δ*Tg*ATS2-HA and parental line using anti-HA and anti-IMC1 shows that Δ*Tg*ATS2-HA has a cytokinetic defect phenotype (scale bars, 2 μm).

(B) IFA of Δ*Tg*ATS2 and parental line transiently expressing MORN1-mCherry (IMC basal tip) and anti-IMC1 (scale bars, 2 μm).

(C and D) Confirmation of enlarged residual bodies in Δ*Tg*ATS2 by IFA using anti-GAP45 (IMC marker) (C) and by statistical analysis of residual body size (D). Scale bars, 2 μm.

(E) IFA observation of extracellular parasites using anti-SAG1 reveals egressed parasites tethered at their basal ends (white arrowhead, PM tether). Scale bars, 2 μm.

(F) Electron microscopic image of Δ*Tg*ATS2 mutants reveals important cytokinesis defects: major enlargement of the PM, defects in mother cell membrane constriction and cell daughter attachment at the basal pole (F1 and F2; enlarged in F1′, F1′′, and F2′, white arrows), and IMC fragmentation at the separation sites between dividing parasites (F2′′). Residual bodies containing unevenly separated nuclei (F1, F3, F3′, F4, and F5), mitochondria (F4, F5, F6, and F6′), and acidocalcisomes (F5). N, nucleus; Mt, mitochondria; rb, residual body; Ac, acidocalcisome. Scale bars, 1 μm.

scavenged from the host, such as C20:4 and C20:5 (Welti et al., 2007; Ramakrishnan et al., 2012; Amiar et al., 2016; Figures S3A and S3B). Comparison of the relative FA abundance between Δ*Tg*ATS2 and its parental line showed significant decreases of C14:0, C20:0, C20:1, and C22:2 (Figure 3C). These results indicate that in addition to the aforementioned cytokinesis defect, Δ*Tg*ATS2 has a highly modified lipid content that relies more on long-chain FAs scavenged from the host (Figures 3A–3C).

To further investigate Δ*Tg*ATS2 lipid defects, we analyzed and quantified each PL class and its individual FA content. The Δ*Tg*ATS2 mutant accumulates significantly more LPA compared with the control parental line and significantly less PA (Figures 3D and 3E), consistent given that LPA and PA are the likely substrate and product, respectively, of ATS2 (Figure 1C). The slight reduction in PA suggests that *Tg*ATS2 is not responsible for the bulk PA synthesis but rather for a specialist function. Importantly, the LPA/PA ratio was significantly affected in Δ*Tg*ATS2 (Figure 3E). We investigated diacylglycerol (DAG) and other related PLs, namely PC, PE, PI, PS, phosphatidylglycerol (PG) and cardiolipin (CL; Figure 3D). The relative abundance of both DAG and PG significantly decreased in Δ*Tg*ATS2 (Figure 3D). This is relevant because DAG can be a direct product of PA, and PG is the sole PL made from PA in plant chloroplasts (Ohlrogge and Browse, 1995). In contrast, the relative abundance of PS, PI, and PE increased in the mutant (Figure 3D).

We then examined the FA profiles of each of these lipid classes. LPA had significant increases in the amounts of C16:0 and C18:0 in Δ*Tg*ATS2 parasites, whereas significant decreases in the apicoplast-specific FAs C12:0 and C14:0 were measured in the mutant (Figure 3F). No major difference was observed in PA composition in Δ*Tg*ATS2 parasites (Figure 3G). Strikingly, though, DAG, PC, PI, and PE all had significantly reduced C14:0 content (Figures 3D and S3C–S3H), which is the main product of FASII and is used by *Tg*ATS1 for bulk *de novo* synthesis of PC, PI, and PE (Amiar et al., 2016). This indicates that *Tg*ATS2 likely uses apicoplast-generated C14:0 as its major substrate to make these lipids. In contrast, the levels of two long polyunsaturated FAs (PUFAs), C20:4 and C20:5, in all three major PLs (PC, PI, and PE) were significantly increased in Δ*Tg*ATS2 (Figures S3C–S3H), which is again consistent with mutant parasites compensating for the lack of *de novo*-made FAs by increasing scavenging long-chain FAs from the host. The FA composition of fetal bovine serum (FBS) and HFF host cells (Figures S3C–S3H) confirmed that C20:4 and C20:5 PUFAs were

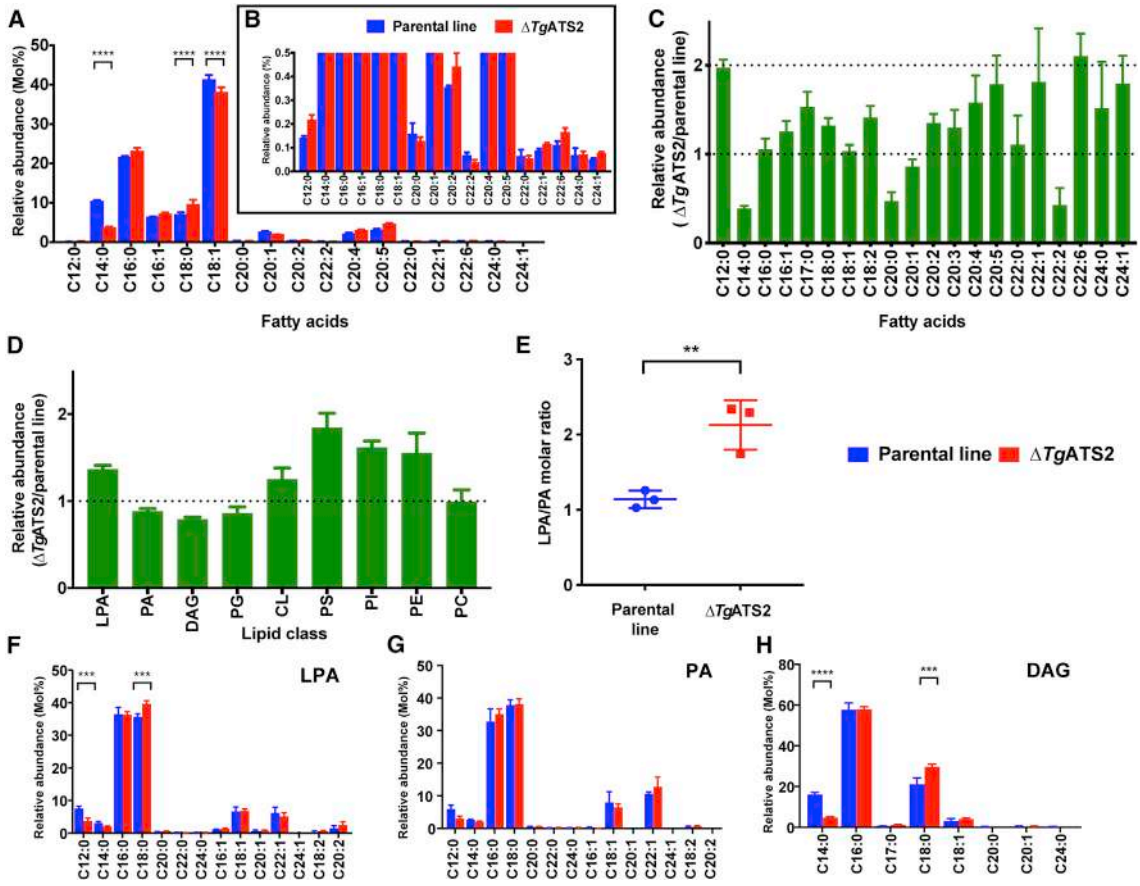

Figure 3. Lipidomic Analysis of Δ*Tg*ATS2 Mutant

(A) Fatty acid composition of total lipid extracted 72 h post-infection.

(B) is enlargement of A.

(C) Relative fatty acid abundance of Δ*Tg*ATS2 to the parental line.

(D) Relative major phospholipid abundance of Δ*Tg*ATS2 to parental line.

(E) LPA/PA ratio.

(F–H) Individual molecular species of LPA (F), PA (G), and DAG (H). Fatty acids are shown as Cx:y, where x is the number of carbons and y is the number of unsaturations.

n = 4; *p ≤ 0.05, **p ≤ 0.01, ***p ≤ 0.001, and ****p ≤ 0.0001.

present from the host environment. This is consistent with the Δ*Tg*ATS2 mutants' increasing scavenging of these PUFAs to make PC, PI, and PE. We complemented Δ*Tg*ATS2 and WT parasites (Figure S3I) using exogenous PA(14:0;14:0), the putative product of *Tg*ATS2, and PA(16:0;18:1) as host-derived PAs. Proliferation assays showed that both exogenous PA sources could significantly boost parasite growth (Figures S3I and S3J) but could not rescue Δ*Tg*ATS2 growth phenotype. This indicates that the PA source needs to be made *de novo* via *Tg*ATS2 for proper division. Because parasites are capable of scavenging lipids from the host and medium, we determined whether the Δ*Tg*ATS2 imported more PA, using PC as a control. Δ*Tg*ATS2 imported significantly more PA and PC than the parental control line (Figure S3K). Together these data on extracellular Δ*Tg*ATS2 corroborate our lipidomic analyses (Figure 3), indicating that the mutant scavenges more lipids to compensate for reduced *de novo* synthesis.

Disruption of *Tg*ATS2 Induces a Mis-localization of the Parasite DrpC Perturbing Parasite Cytokinesis, IMC Formation, and PM Stability

Lipidomic analyses revealed a drastic LPA/PA imbalance in the Δ*Tg*ATS2 mutant (Figure 3E). LPA and PA have important structural influences on membrane architecture and endocytosis by inducing local membrane curvatures, which can affect the recruitment and functions of specific dynamins at precise membrane domains for organelle/vesicle fission (Adachi et al., 2016; Schmidt et al., 1999; Gras et al., 2019). For example, synaptic vesicle transport between neurons requires a protein complex composed of a dynamin and an endophilin that exert acyltransferase activity to create the proper membrane groove where the dynamin can pinch and release the synaptic vesicle, or in human mitochondrial fission by the protein Dynamin-like 1, *Hs*Drp1, which requires insertion, recruitment, and regulation through PA. In *T. gondii*, there are three known dynamin-related

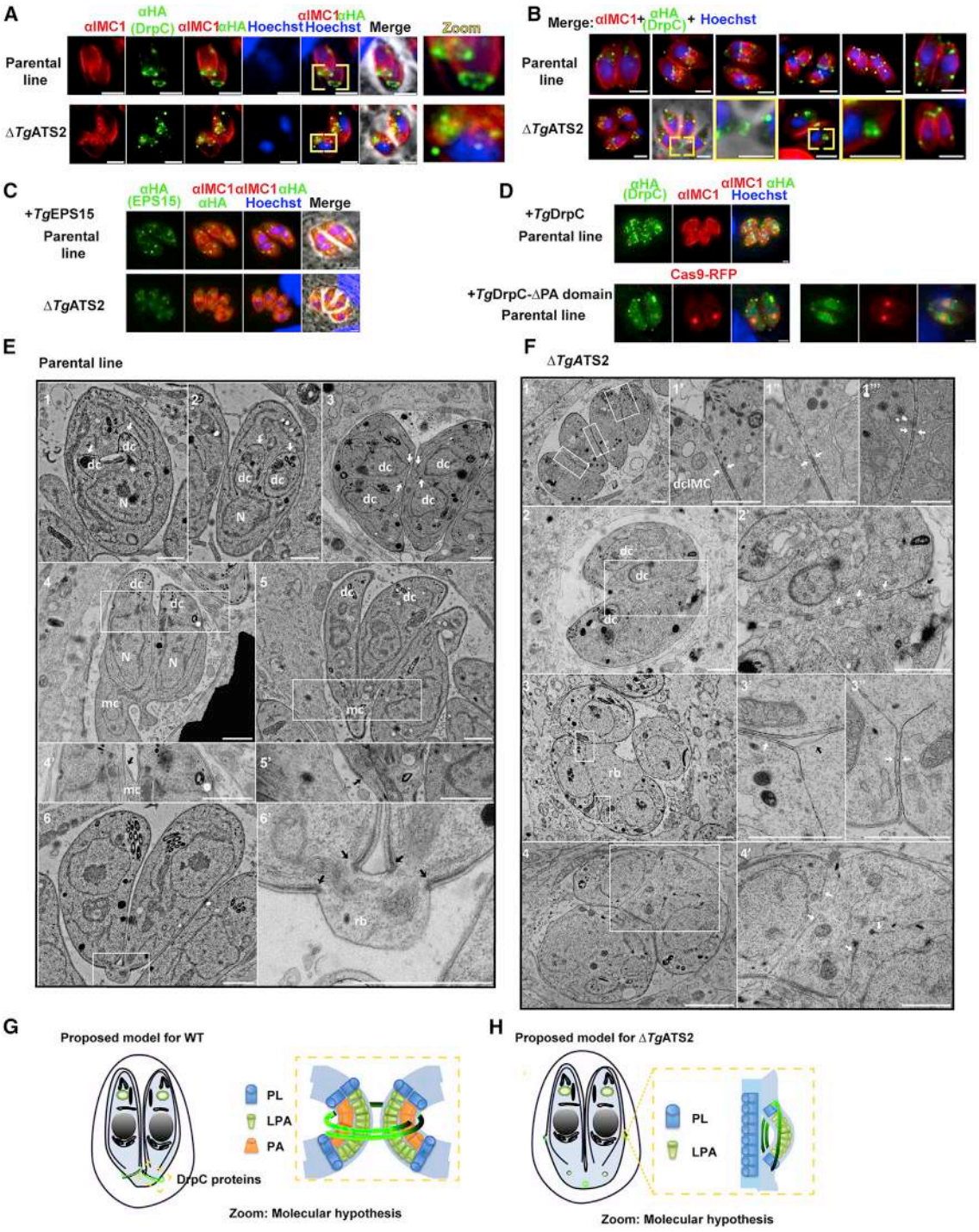

Figure 4. Δ*Tg*ATS2 Induces the Specific Mis-localization of *Tg*DrpC, a Dynamin-Related Protein Involved in Endodyogeny, Leading to Cytokinetic Defects during Tachyzoite Division

(A) IFA localization of *Tg*DrpC-HA expressed in parental line shows ring structures at the growing ends of daughter cells during division (top panel) but fails to do so when expressed in Δ*Tg*ATS2 (bottom panel). Scale bars, 2 μm.

(B) *Tg*DrpC-HA localization during tachyzoite division cycle in the parental line (top panel) and its mis-localization in Δ*Tg*ATS2 mutant. Scale bars, 2 μm.

(C) IFA localization of TgESP15, a known interactor of TgDrpC, in Δ*Tg*ATS2 and parental line using anti-HA and anti-IMC1. Scale bars, 2 μm.

(D) IFA localization of *Tg*DrpC and *Tg*DrpC-ΔPA domain-Cas9-RFP using anti-HA and anti-IMC1 (scale bars, 2 μm) reveals the mis-localization of TgDrpCΔPA domain during endodyogeny.

(legend continued on next page)

proteins (Drps): *Tg*DrpA, *Tg*DrpB, and *Tg*DrpC. *Tg*DrpA and *Tg*DrpB have roles in apicoplast fission and secretory organelle biogenesis, respectively (van Dooren et al., 2009; Breinich et al., 2009). *Tg*DrpC was recently localized to the basal poles of dividing daughter cells (Heredero-Bermejo et al., 2019). We generated a parasite line expressing *Tg*DrpC fused to a 3xHA tag under the control of its endogenous promoter using CRISPR-Cas9 (Figures S4A and S4B) and localized *Tg*DrpC-HA during the tachyzoite intracellular division cycle in Δ*Tg*ATS2 and its parental line (Figure 4A). In parental-line parasites, *Tg*DrpC-HA clustered in small punctate-like compartments in the apical post-Golgi area during interphase (Figure 4A). During daughter budding, *Tg*DrpC re-localized to form two distinct ring-like structures coinciding with the growing ends of the IMC from the budding daughter cells, which constricted at the base of the mother cell during cytokinesis and eventually formed basal caps on the each newly divided parasite (Figures 4A and 4B).

In Δ*Tg*ATS2, localization of *Tg*DrpC-HA was only mildly affected during interphase but was drastically affected during division (Figures 4A and 4B). Indeed, *Tg*DrpC-HA frequently failed to form the typical ring structures at daughter cells (Figures 4A and 4B). Instead, DrpC-HA was scattered in the cytosol, or formed rings pushing on the side of mother IMC, or improperly constricted at the daughter basal pole (Figures 4A and 4B). This contrasted with the normal localization of MORN1, which appears to be a more cytoskeletal component, as its localization remains unaffected during endodyogeny (Figure 2B). We further examined other known interactors of DrpC and thus localized the dynamin-like protein EPS15 (Heredero-Bermejo et al., 2019) by C-terminally tagging by CRISPR-Cas9 (Figures 4C and 4D). In parental strains, EPS15-HA localized to clear punctate dots during interphase similarly to DrpC. During endodyogeny, EPS15 remained as punctate dots and did not re-localize to the daughter rings like DrpC (Figure 4C). In Δ*Tg*ATS2 background, EPS15 was unaffected during interphase though more scattered than in the parental line. However, during endodyogeny, EPS15-HA mis-localized in the cytosol of the parasite when expressed in the Δ*Tg*ATS2 background (Figure 4C), consistent with its role as a DrpC interactor (Heredero-Bermejo et al., 2019).

In silico sequence alignment showed that (1) *Tg*DrpC is the closest *Tg*Drp homolog to the *Hs*Drp1, which allows mitochondrial fission through its interaction with PA via its Stalk domain including a loop with specific hydrophobic residues (Adachi et al., 2016, 2018), and (2) the Stalk domain and the PA binding loop seem conserved in *Tg*DrC (3) but are absent in *Tg*DrpA and *Tg*DrpB (Figures S4C–S4E). To confirm this, we tagged and monitored the localization of other *Tg*Drps in the Δ*Tg*ATS2 background. No obvious change in localization of *Tg*Drp*A* was observed in Δ*Tg*ATS2 parasites, even during the fission of the apicoplast (Figure S4B).

On the basis of homology with *Hs*Drp1, we disrupted the putative PA-binding region of *Tg*DrpC. We expressed this *Tg*DrpC-ΔPA version of the protein in the parasite to test the importance of the putative PA-binding domain for the localization of *Tg*DrpC. To do so, we transfected a WT *Tg*DrpC-HA cell line with a Cas9-RFP and a PCR product targeting the DrpC PA domain. IFAs on parasites with no Cas9-RFP had typical DrpC-HA localization (Figure 4D). However, parasites with positive Cas9-RFP expression showed that DrpC was mis-localized and scattered throughout the cytosol in a similar manner as in *TgΔATS2* parasites. These results are also consistent with the cytosolic mis-localization of truncated *Tg*DrpC, excluding the putative PA-binding domain recently reported (Melatti et al., 2019).

Further detailed evidence of improper cytokinesis could be observed under EM. In the parental line, initial steps of endodyogeny showed the formation of the daughter cell apical pole along with organelle division before the formation of the daughter cells within the mother cell (Figure 4E). Emergence of the daughter cells initiates the apical-to-basal biogenesis of their PM, partly recycled from the mother (Figures 4E1–4E5), and ends by a constriction of both IMC and PM at the basal poles, leaving a small basal residual body (Figure 3F6). IMC biogenesis and aberrant endocytosis can be seen in *TgΔATS2* cells upon closer inspection under EM. In contrast Δ*Tg*ATS2 were unable to separate, although a new round of daughter formation could be initiated (Figure 4F1). Daughter cells were found tightly apposed at normal emergence sites, and their PMs were often missing between daughter IMCs. Instead, interconnection of PM, vesicles, or cisternae could be observed at these apposition sites and at the basal end of dividing cells (Figures 4F1 and 4F2). Mother cells were frequently observed to be fused to each other, with vesicle fusion frequently occurring between the two at the site of the PM (Figure 4F2). These defects suggested issues at the PM composition and/or problems in membrane fusion/fission sites. Furthermore, there was no constriction of both IMC and PM from daughter cells, resulting in enlarged residual bodies containing organelles and cytosol portions (Figures 4F3 and 4F4). In particular, these membrane invaginations were frequently seen at the junction between two parasites in a process resembling endocytosis.

(E and F) Electron microscopic observation of endodyogenic division in parental line (E) and ΔTgATS2 (F). (E1–E3) Endodyogeny starts with the formation of daughter cells (dc) by growth of IMC (white arrows) and organelle segregation. IMC scaffolding then grows toward the basal pole (white arrows) encompassing divided organelles (e.g., nucleus N). (E4–E5′) Recycling and biogenesis of PM (black arrow) ends daughter cell emergence from mother cell (mc). (E6 and E6′) Division ends by cytokinesis through constriction of both IMC and PM at basal pole (black arrows) to form a small residual body (rb). (F) Δ*Tg*ATS2 shows an incomplete separation of daughter cells during cytokinesis with absence of PM biogenesis between closely apposed IMC (F1 and F3 and insets, white arrows), presence of vesicle/cisternae inside membrane structures at the inter-IMC space (F2′, white arrows), absence of mother IMC (F3′, black arrow), absence of basal constriction forming large residual bodies leaving floating daughter IMC (F3, F4, and 4′, white arrows). Scale bar, 1 μm.

(G and H) Proposed molecular model for *Tg*DrpC function during endodyogeny and cytokinesis in WT parasite (G) and Δ*Tg*ATS2 (H). LPA and PA molecules induce positive and negative curvature, creating grooves in membranes for *Tg*DrpC to insert at specific sites during division for a pinching function during endodyogeny (G).

Nutrient Starvation Enhances the Synthesis of FA by Apicoplast FASII in *T. gondii* and Blocks Intracellular Proliferation of *P. falciparum* Blood Stages Lacking a Functional FASII

Because *Tg*ATS2 has a role in maintaining parasite lipid homeostasis, we set out to determine the balance of *de novo* synthesized versus scavenged lipids in Δ*Tg*ATS2 using a stable isotope precursor of apicoplast synthesized FAs, U-^{13}C-glucose. (Ramakrishnan et al., 2012; Amiar et al., 2016; Dubois et al., 2018). Incorporation of ^{13}C within FA is detected by increase of mass and determined in relation to non-labeled FA. Distribution of ^{13}C incorporation to each FA isotopologue is shown as its own mass (M) plus number of ^{13}C carbon incorporation (i.e., M + x). In both parental and Δ*Tg*ATS2 mutant lines, we observed significant differences of ^{13}C incorporation in C14:0, C16:1, C18:0, and C18:1 (Figure 5A). Isotopologue distribution of apicoplast-signature C14:0 showed that Δ*Tg*ATS2 had ^{13}C incorporation up to M + 14, but major incorporation occurred at lower masses (M + 8, M + 10) than the parental (M + 12, M + 14; Figure 5B). This indicates that FASII is active in Δ*Tg*ATS2 but slowed down in the process of making C14:0, thus explaining the C14:0 reduction previously detected (Figure 3A). Similar significant results were observed for C16:0 isotopologue distribution, although overall incorporation was similar between parental and Δ*Tg*ATS2 (Figure 5C). C18:0 in Δ*Tg*ATS2 had higher ^{13}C incorporation than the parental, and its isotopologue distribution showed more short FA from the apicoplast (Figure 5D).

Lipidomic analyses thus indicate that both scavenged and *de novo* lipid fluxes are modified in Δ*Tg*ATS2. To tease out the impact of host nutritional environment on both pathways, we sought to measure parasite lipid fluxes under adverse host nutritional/lipid conditions, through limitations in FBS concentrations in parasite culture media. Interestingly, gas chromatography-mass spectrometry (GC-MS) analysis revealed that ^{13}C incorporation into all FASII-generated and further ER-elongated FA products (i.e., C14:0, C16:0, C16:1, C18:0, C18:1, and C20:1) was significantly higher by 5%–15% under FBS starvation in the parental line (Figures 5E, 5F, and S5A). In addition, ^{13}C incorporation into most FAs is increased in the WT parental line (Figure 5F). These results suggest that apicoplast *de novo* FA/lipid synthesis can be upregulated during FBS starvation to compensate for the lack of nutrients in the external environment. However, in Δ*Tg*ATS2, the ^{13}C incorporation into each FA was decreased by FBS starvation (Figure 5F). No morphological changes could be observed by IFA in the FBS-starved WT or Δ*Tg*ATS2 mutant (Figure S5B). Both parental line and Δ*Tg*ATS2 mutant showed a significant reduction in the synthesis of C18:0 in FBS-starved conditions, suggesting that C18:0 is obtained predominantly by scavenging from the host cell (Figure 5F). Because the availability of lipids from the environment is limited, the FA abundance in the parental line was decreased (Figure 5G). Interestingly however, the FA abundance in Δ*Tg*ATS2 was increased in most of its FA species during FBS starvation (Figure 5G).

Although we observed a defect in the activation of FASII in Δ*Tg*ATS2, FASII was nevertheless viable during FBS starvation. This suggests that if FASII is active, regardless of the level of FASII activity, the parasites are viable under FBS starvation, consistent with its essential role in tachyzoites. However, in *P. falciparum*, FASII is not essential during nutrient-replete blood stage but is activated under lipid starvation, apparently to compensate for reduced availability of scavenge-able lipids (Yu et al., 2008; Botté et al., 2013). Our results in *T. gondii* led us to re-think the current hypothesis regarding the dispensability of the apicoplast FASII in *P. falciparum* blood stages and to test the essentiality of malaria parasite apicoplast FASII under nutrient/lipid-starved conditions. We grew *P. falciparum* FASII KO, Δ*Pf*FabI (Yu et al., 2008), and its parental line (NF54) in either regular (i.e., lipid-rich) culture medium or in "lipid-starved" minimal medium (Mi-Ichi et al., 2007; Botté et al., 2013). Both NF54 and Δ*Pf*FabI grew normally in the regular culture medium (Figure 5H). In the lipid-starved medium, NF54 was viable but grew significantly slower than in lipid-replete conditions, as previously reported (Shears et al., 2017). However, Δ*Pf*FabI grew only for the first 2 days in lipid-starved media, but after 4 days, a sharp decrease in growth occurred, and this led to a complete loss of detectable parasites after 8 days and showed no sign of further recovery in the next monitored cycles (Figure 5H). This shows that FASII is required for the malaria parasite blood stages to adapt its lipid metabolism in response to an adverse host lipid environment, a similar situation to that revealed here for *T. gondii*.

Because environmental FBS starvation induces an increase of *de novo* lipid synthesis, we investigated the effect the lipid-nutrient-depleted conditions (i.e., 0%, 1%, and 10% of FBS) on various mutants involved in lipid metabolism in *T. gondii*. We assessed parasite growth by plaque assay and quantified plaque area. The WT and parental parasite lines could grow equally well in DMEM supplemented with 0%, 1%, or 10% FBS (Figures 5I–5R and S5C), without affecting the integrity of HFF host cells. FBS starvation reduced growth of Δ*Tg*ATS2 under 0% FBS (Figure 5I). *Tg*ATS1-depleted cells grew sharply less in the regular culture conditions (i.e., 1% FBS), but starvation under 0% FBS led to the quasi-absence of plaques, whereas an increase to 10% FBS partially rescued the growth defect seen in 1% FBS (Figure 5J). This suggested that in the absence of the major *de novo* PL precursor synthesis pathway, the parasite could partially compensate the growth defect by accessing more host lipid resources. The acetyl-CoA synthetase *Tg*ACS (Dubois et al., 2018) was adequately responsive to FBS starvation (Figure 5K). Interestingly, proteins not involved in bulk membrane/lipid synthesis, such as *Tg*PKA-iKO, could not be rescued by excess nutrients (Figure 5L; Uboldi et al., 2018).

Because host FA binding proteins (FABPs) are upregulated upon tachyzoite invasion (Hu et al., 2017), we searched the genome of *T. gondii* for homologs of FABPs that could be responsible for the transport of FAs in the parasite during starvation but found none. Instead, we found two proteins belonging to the closely related family of acyl-CoA binding protein (ACBP): *Tg*ACBP1 and *Tg*ACBP2. We found that *Tg*ACBP1 and *Tg*ACBP2 localized at the parasite cytosol and mitochondrion, respectively (Figures S5D–S5G). We generated inducible knockdown parasite lines for both (Figures S5D and S5E). However, plaque assays showed that both proteins were dispensable during tachyzoite life stages, and neither was responding to FBS starvation (Figures 5M and 5N), suggesting that neither of the

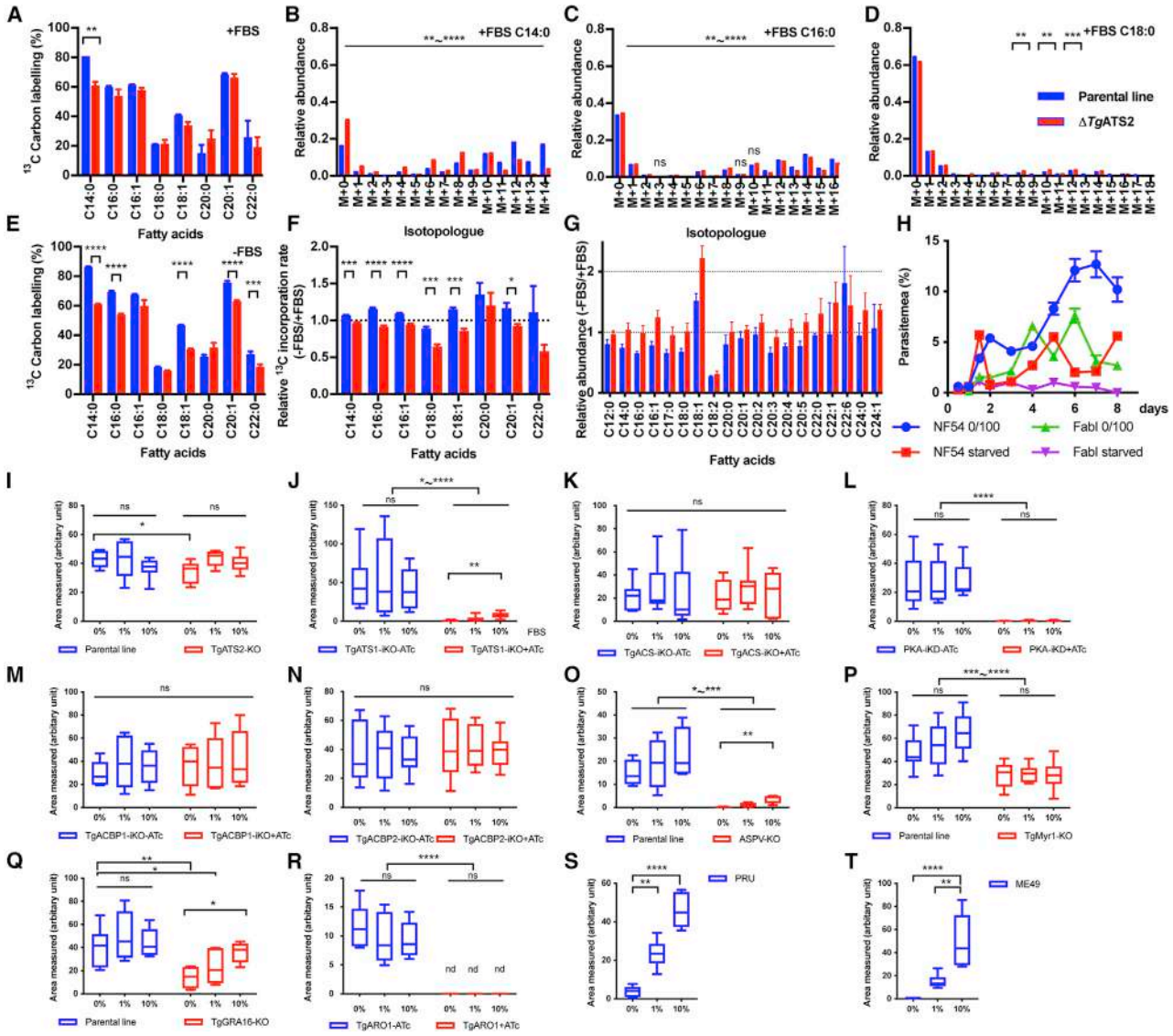

Figure 5. Changes in Host Nutritional Environment Induces an Upregulation of the Apicoplast FASII Metabolic Capacities in *T. gondii* Tachyzoites and *P. falciparum* Blood Stages and Are Pivotal for Enzymes Involved in Metabolic Adaptation

(A–G) U-^{13}C-glucose labeling for 72 h to monitor apicoplast FA synthesis by ^{13}C incorporation to fatty acids (blue, parental line; red, Δ*Tg*ATS2). (A) ^{13}C incorporation to each fatty acid in 1% FBS. (B–D) Mass isotopologue distribution in 1% FBS for C14:0 (B), C16:0 (C), and C18:0 (D). The x axis shown as "M + X" represents mass with "X" ^{13}C atoms incorporated during the FA synthesis. (E) ^{13}C incorporation to each fatty acid in 0.2% FBS. FASII metabolic activity increased upon FBS starvation in the parental line but not in Δ*Tg*ATS2. (F) Change in ^{13}C incorporation between 0.2% FBS and 1% FBS (−FBS/+FBS). (G) The relative abundance of each FA (−FBS/+FBS).

(H) Asexual blood stage growth assay of *P. falciparum* FabI-KO and its parental line (NF54) in regular (lipid-rich) culture medium and lipid-starved medium reveals that FASII is essential in blood stage in low-lipid environment.

(I–T) Growth assays conducted in 0%, 1%, or 10% FBS in different *T. gondii* mutants and strains: *Tg*ATS2 (I), *Tg*ATS1 (J), *Tg*ACS (K), *Tg*PKA (L), *Tg*ACBP1 (M), *Tg*ACBP2 (N), *Tg*ASP5 (O), *Tg*Myr1 (P), *Tg*GRA16 (Q), *Tg*ARO1 (R), type II PRU (S), and type II ME49 (T).

$n \geq 3$. ns, not significant; *$p \leq 0.05$, **$p \leq 0.01$, ***$p \leq 0.001$, and ****$p \leq 0.0001$.

*Tg*ACBPs is involved as an effector for the adaptation to nutritional environment. We generated a *Tg*ACBP1 and *Tg*ABCP2 double KO and a double ACBP1iKD/sterol carrier protein (SCP2) KO cell line, which we also found to be viable and not responsive to starvation (Figures S5H and S5I).

We then hypothesized that parasite effectors putatively exported into the PVM or toward the host cell could be used by the parasite to collect putative host membrane material generated during FBS starvation. To test this, we investigated *Tg*ASP5, a Golgi-resident aspartyl protease that controls the non-canonical trafficking pathway of parasite effectors toward the PVM and the host cell, during FBS starvation (Bougdour et al., 2014). Strikingly, FBS starvation significantly exacerbated the growth defect in Δ*Tg*ASP5 (Figures 5O and S5). By contrast,

the mutant cell line Δ*Tg*MYR1 (the canonical system to export effectors toward the host; Franco et al., 2016) showed overall less growth than the parental cell line, although Δ*Tg*MYR1 grew equally well among the 0%, 1%, and 10% FBS conditions (Figure 5P). To examine the effects of some specific GRA effectors, we examined a GRA16-KO cell line, which we observed to have a minor but significant growth defect under FBS starvation, suggesting that at least some GRA proteins are important, likely in combination (Figure 5O). We also examined a mutant for rhoptry secretion *Tg*ARO-iKO (Mueller et al., 2013) but found that under ATc treatment, the mutant died regardless of FBS concentration (Figure 5R), suggesting a primary role in host invasion prior to host re-wiring.

Last, we explored strain-specific differences between in *Toxoplasma* between the hypervirulent type I RH strain and type II strains (Prugniaud, ME49) capable of forming chronic stages (bradyzoites). Both type II strains showed significantly reduced growth in lipid-depleted medium (Figures 5S and 5T), unlike type I strain.

Together, these data provide evidence that in response to nutrient starvation, parasite effectors can be trafficked to the host cell, primarily via the *Tg*ASP5 export pathway, likely to enhance the ability to scavenge resources.

Nutrient Starvation Induces the Formation of Multi-membrane-Bound Vesicles in Host Cells that Are Taken up by the Parasite

To investigate potential changes to the host cell and hence host-parasite interactions during lipid starvation, we performed EM on starved (0%, 1%, or 10% FBS) HFF host cells infected with either the parental parasite line or Δ*Tg*ATS2. Growth in 10% FBS led to no obvious phenotype changes in the hosts cells or the parental parasite line or the Δ*Tg*ATS2 mutant (Figures 6A and 6B), but reduction to 1% and 0% FBS induced striking changes in the host cells, which became extensively vesiculated irrespective of whether they were infected with the parental line or Δ*Tg*ATS2 (Figures 6A and 6B). Such vesiculation was not observed in uninfected HFF host cells put under nutrient starvation. Giant multi-vesicular bodies (gMVBs; i.e., large membrane-bound compartments containing various smaller vesicles) were frequent in 1% FBS-grown cells (Figures 6A and 6B) and very numerous at 0% FBS (Figures 6A and 6B). The gMVBs are distinct from host autophagosome, as they lack the typical double/multiple surrounding membranes and the cytosolic material defining autophagosomes (Ylä-Anttila et al., 2009). This was confirmed by IFA using the typical autophagosome marker anti-LC3, which showed no accumulation of autophagosome under 10%, 1%, or 0% FBS (Figure S6). The gMVBs could arise from the host ER, as the ER could be seen swelling and forming networks containing large lipid bodies (Figure 6B3). gMVBs were also often seen in close apposition or contact with the mitochondria and/or ER network, indicating that material could also be transferred from both (Figures 6B3 and 6B5). However, gMVBs were more often observed arising directly from the host nuclear envelope, potentially a major contributor to their formation (Figures 6B6–6B8). The gMVB accumulated in close vicinity with the PVM, which houses the parasite during its intracellular development and serves as the exchange interphase between the host and the parasite. The gMVBs were not only close to the PVM but appeared to be interacting with the PVM with host material and vesicles from the gMVB, apparently "percolating" through the PVM (Figure 6B4) or directly from their originating organelles (Figure 6B5) to eventually be found in the PVM (Figures 6A and 6B1). These vesicles appeared in both WT and Δ*Tg*ATS2, suggesting that the host cell is responding to the nutrient deficiency in the same way. The Δ*Tg*ATS2 parasite cytokinesis phenotype (e.g., Figure 2A) was still observed and apparently exacerbated in 0% and 1% FBS growth medium (Figure 6B). This vesicle/gMVB formation and trafficking to and within the PVM was not apparent in high (10%) FBS medium, suggesting that host gMVBs somehow allow the parasite to increase its lipid scavenging in the absence of nutrient rich serum. Together this indicates that gMVBs contain multiple vesicles that (1) are dependent and induced by nutrient availability and (2) originate directly from diverse host organelles. The gMVBs are distinct from lipid droplets of host cell origin used as a lipid source by *T. gondii* (Nolan et al., 2017; Romano et al., 2017).

However, it is possible that FBS starvation leads to increased host cell lipid droplet import. Nile red staining confirmed that FBS starvation induced a significant increase of the amount of lipid droplets into the parasites and its PVM (Figure 6C). In contrast, low FBS content resulted in a reduced amount of lipid droplets in uninfected host cells, while high FBS content increased their presence in the host cells alone (Figure 6D). This further indicates that increase of import of lipid droplets to the parasite is upregulated by the parasite during FBS starvation.

Because gMVBs also seem to arise from host mitochondria, we used an anti-lyso-bi-PA (LBPA; i.e., a degradation product of mitochondrial CL) antibody (Kobayashi et al., 1998), a lipid that can also be scavenged by intracellular parasites (Romano et al., 2017; Figure 6E). LBPA was found surrounding the PVM in the host cell, within the PV and the parasite, but its localization and intensity remained unchanged in response to reduced FBS content (Figure 6E). Direct salvage of mitochondrial CL per se might not be the primary upregulated scavenging pathway during lipid starvation.

To determine whether host mitochondrial sequestration could affect parasite adaptation to low host nutrient, we measured the levels of mitochondrial sequestration in type I parasites (prone to host mitochondrial sequestration) and type II parasites (not sequestering host mitochondria) (Pernas et al., 2014). Host mitochondria was monitored with MitoTracker. Both RH type I and type II ME49 parasites showed no major difference in host mitochondrial sequestration after FBS starvation (Figure S6).

DISCUSSION

We have shown that *Tg*ATS2 is an apicoplast acyltransferase able to esterify FAs on LPA to generate PA, a precursor for a wide range of parasite lipids. KO of *Tg*ATS2 resulted in perturbed lipid fluxes, which affects LPA/PA lipid balance, causing mislocalization of *Tg*DrpC and vesiculation during cytokinesis. Furthermore, changes in lipid profiles of Δ*Tg*ATS2 showed the capacity of WT parasites to exhibit considerable metabolic plasticity at both *de novo* FA synthesis in the apicoplast and host modification for organelle membrane scavenging, together

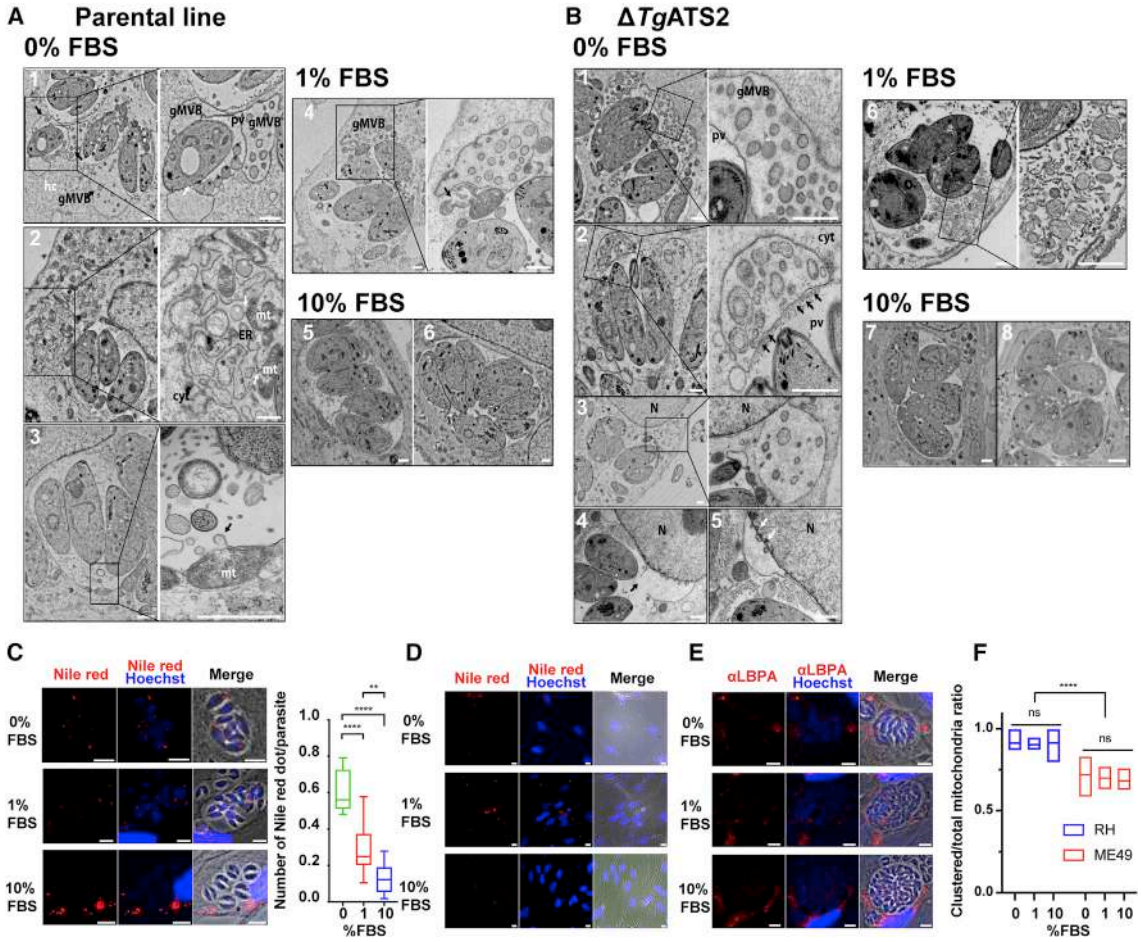

Figure 6. Nutrient Starvation Unveils the Formation of Multi-vesicular Bodies from Host Cell Organelles, Whose Content Is Imported toward Parasites

(A and B) Transmission electron micrographs of intracellular WT tachyzoites (A) and Δ*Tg*ATS2 mutant parasites (B) grown in 0%, 1%, and 10% FBS. Nutrient starvation (i.e., 0% and 1% FBS) induces formation of giant multi-vesicular bodies (gMVBs) in the host cell (hc), containing various vesicles, including lipid body-like (white stars). In starvation, gMVBs localized in the cytosol (cyt) in contact with the parasitophorous vacuole (pv) (A1, A2, A4, B1, and B2), and their content was imported through and into the PV (A1, black stars; B2 and B6, black arrows); gMVBs were arising from host endoplasmic reticulum (ER; A2), mitochondria (mt; A2 and A3), and mainly swollen nuclear envelope (N; B3–B5). Ten percent FBS did not induce gMVB formation in both parental and Δ*Tg*ATS2. Scale bar, 1 μm.

(C) Nutrient starvation induces a significant increase of lipid droplets within the parasite and its PV as measured by IFA using Nile red (Nile red dots were counted for 100 or more parasites; n = 3; ns, not significant; *p ≤ 0.05, **p ≤ 0.01, ***p ≤ 0.001, and ****p ≤ 0.0001). Scale bar, 2 μm.

(D) Nutrient starvation induces a decrease of lipid bodies in uninfected HFF host cells as measured by IFA using Nile red. Scale bar, 2 μm.

(E) IFA shows that import into parasites of LBPA (anti-LBPA) is not affected by nutrient starvation. Scale bar, 2 μm.

(F) Nutrient starvation induces a significant growth defect in *T. gondii* tachyzoites ME49 type II strain compared with RH type I strain. p values are as mentioned as above.

critical for adaptation to nutrient-limiting conditions in the host (Figure 7; Table S1).

Roles of PA and LPA in Membrane Curvature and Cell Division

Membrane PLs have different physical shapes according to the relative sizes between the polar head and the FA tails. Most PLs are cylindrical, while PA is cone shaped and LPA adopts an inverted cone shape; thus their insertion into membrane bilayers facilitates curvature and in- or evagination (Kooijman et al., 2005).

Furthermore, in human cells, dynamin pinching requires endophilin-1, an ATS2 homolog, as a partner to create LPA/PA curvatures (Burger et al., 2000; Shin and Loewen, 2011), improving penetration of a larger part of dynamin into the lipid monolayer (Burger et al., 2000; Shin and Loewen, 2011), similar to the relationship between *Tg*ATS2 and *Tg*DrpC. Our results reveal the previously unrecognized importance of the apicoplast in maintaining internal lipid homeostasis. Furthermore, the functional role of *Tg*ATS2 for PA synthesis during division provides a mechanism for the long-standing question of why drugs targeting the apicoplast display a secondary cytokinetic defect (Martins-Duarte et al., 2015).

Our results nicely complement those of a recent study that identified the basal complex as a major site of endocytosis in

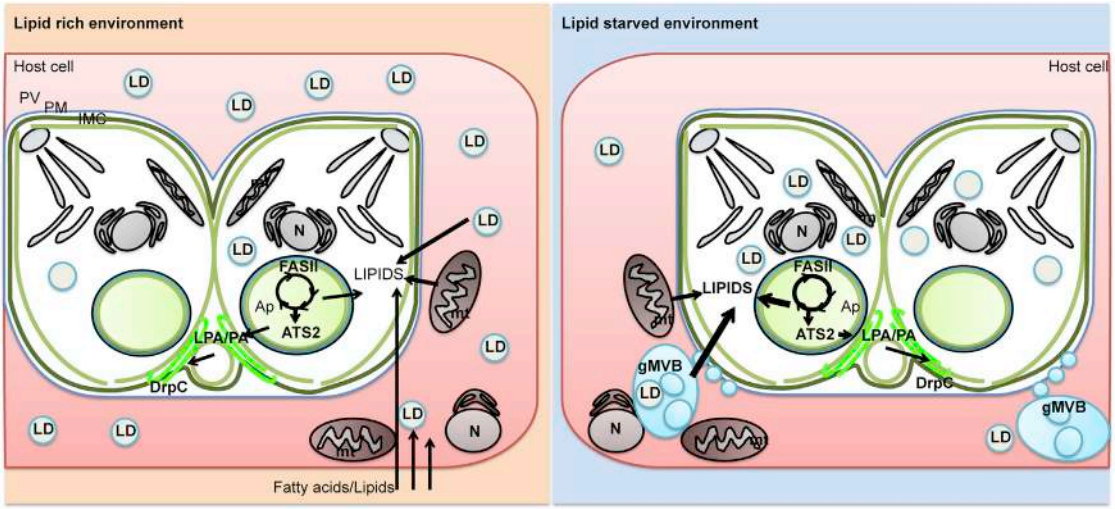

Figure 7. Proposed Model for Cytokinesis, Lipid Acquisition, and Metabolic Adaptation under Adverse Host Lipid Environment in *T. gondii*

Left: under lipid-rich environment, *T. gondii* can readily acquire FAs and lipids by *de novo* synthesis (apicoplast) and host cell scavenging. The apicoplast ATS2 generates PA and regulates the balance of LPA/PA, necessary for DrpC. Right: in a host lipid-starved environment, the parasite adapts its metabolism by increasing FASII to produce more fatty acids to compensate their absence from the host cell. Concomitantly, the parasite induces morphological changes in the host to increase scavenged resources, including the nucleus, ER, and gMVBs.

motile tachyzoites, consistent with the basal complex localization of DrpC (Figure 4; (Heredero-Bermejo et al., 2019). Our results show that endocytosis occurs during intracellular stages and that aberrant LPA/PA ratios caused by the loss of ATS2 disrupt this process.

Furthermore, many DrpC-interacting proteins have been identified as part of a larger endocytic protein complex, including EPS15, AP2 adaptins, and, intriguingly, Kelch13 (Heredero-Bermejo et al., 2019). Kelch13 is the infamous protein found mutated in artemisinin-resistant malaria spreading throughout Asia (Menard and Dondorp, 2017). Kelch13 therefore likely has a role in endocytosis consistent with DrpC and other interacting partners (Heredero-Bermejo et al., 2019). Intriguingly, it has been shown that FASII activity is often increased in artemisinin-resistant parasites (Chen et al., 2014). Our evidence here demonstrates that the upregulation of FASII produces LPA that modulates cytokinesis and endocytosis processes. Again, this highlights the previously unrecognized importance of the apicoplast in maintaining internal lipid homeostasis in parasites.

Environmental and Nutritional Conditions Drive the Adaptation of the Apicoplast Metabolic Capacities as Well as the Scavenging Capacities

Importantly, *Toxoplasma* could increase production of FA in the FASII pathway in nutrient/lipid-deprived medium similarly to *P. falciparum* (Botté et al., 2013). Hence, apicomplexan parasites show high metabolic flexibility to obtain FA for the major membrane building blocks required for growth, as pointed out by recent studies exploring *Plasmodium* survival in nutrient-depleted conditions (Mancio-Silva et al., 2017; Zuzarte-Luís et al., 2017). Importantly, our results demonstrate that *P. falciparum* lacking a FASII and grown in lipid-deprived conditions was unable to properly proliferate, ultimately dying. This suggests that apicoplast FASII is facultative rather than totally dispensable in malaria parasite blood stage and can be activated during lipid starvation to meet PL needs. This FASII flexibility is consistent with a growing pool of evidence including the upregulation of FASII and the apicoplast acyltransferase PfG3apiGPAt (a homolog of *Tg*ATS1) transcripts in starved patients (Daily et al., 2007) and the essentiality of most FASII enzymes, including the central acyl-carrier protein ACP in both *T. gondii* and *P. falciparum* (Sidik et al., 2016; Zhang et al., 2018), summarized in Table S1. Therefore, environmental factors could have important consequences in treating patients. Indeed, if patients are under stress, nutrient deprivation, or malnourished conditions, the FASII pathway could become a secondary target of choice to help eradicate the parasites. Altogether these data question whether isopentenyl pyrophosphate (IPP) synthesis is the sole essential function of the apicoplast during *Plasmodium* blood stage (Yeh and DeRisi, 2011). Rather, our data put the parasite back into its physiological context, where nutrient availability and environmental conditions drive the requirement and regulation of a given metabolic pathway. Furthermore, the scavenging of *Toxoplasma* can also be seen to be upregulated through exported effectors by evidence that ASP5 KO is partially rescued by excess host lipids and the induction of host remodeling to make gMVBs, although the identity of these gMVBs warrants further investigation. This redefines what we call an essential gene, where phenotypes might only be seen under starvation conditions.

A major question raised here is the nature the signaling factor(s) responsible for environmental sensing and metabolic adaption of both apicoplast *de novo* synthesis and scavenging pathways. Both *T. gondii* and *P. falciparum* lack the canonical mTOR-based nutrient-sensing pathways present in other eukaryotes, but a recent study showed that *P. berghei* is capable

of sensing nutrient deprivation by a SNF1-related kinase, KIN1 (Mancio-Silva et al., 2017).

Together, our results reveal the central role of the apicoplast to provide specific precursors for membrane biogenesis during cytokinesis and, most important, to be a central metabolic hub to adapt the parasite metabolic capacities upon nutrient availability and environmental changes. The data also point to major modifications in vesiculation and the use and scavenging of these membrane structures by the parasite upon such environmental changes. The data also corroborate recent results showing that the mosquito lipid environment regulates the metabolic activity of transmissible sporozoites (Costa et al., 2018). The fundamental role of these physiological changes induced by the parasite in response to host environment provides novel insights into parasite biology and offers new avenues to explore in the fight against toxoplasmosis and malaria.

STAR★METHODS

Detailed methods are provided in the online version of this paper and include the following:

- KEY RESOURCES TABLE
- MATERIALS AND METHODS
- LEAD CONTACT AND MATERIALS AVAILABILITY
- EXPERIMENTAL MODEL AND SUBJECT DETAILS
  - T. gondii culture
  - P. falciparum culture
- METHOD DETAILS
  - Gene identification and sequence analysis
  - T. gondii plasmid constructs
  - T. gondii transfection
  - T. gondii growth assays
  - T. gondii Red/Green parasite invasion assay
  - Plasmodium falciparum growth assays
  - Immunofluorescence assay and Microscopy
  - Nile red staining of lipid droplets
  - Activity analysis in LPAAT-deficient *E. coli* strains
  - Transmission electron microscopy
  - Lipidomic analysis by GCMS extraction from T. gondii tachyzoites
  - Stable isotope labeling of T. gondii
  - Phospholipid import assay
- QUANTIFICATION AND STATISTICAL ANALYSIS
- DATA AND CODE AVAILABILITY

SUPPLEMENTAL INFORMATION

Supplemental Information can be found online at https://doi.org/10.1016/j.celrep.2020.02.072.

ACKNOWLEDGMENTS

We would like to thank Prof. Alan Cowman and Dr. Ali Hakimi for sharing parasite strains, reagents, and fruitful advice. This work and C.Y.B., Y.Y.-B., S.A., N.J.K., and C.B. are supported by Agence Nationale de la Recherche, France (grant ANR-12-PDOC-0028, Project Apicolipid), the Atip-Avenir and Finovi programs (CNRS-INSERM-FinoviAtip-AvenirApicolipid projects), and Laboratoire d'Excellence Parafrap, France (grant ANR-11-LABX-0024). C.Y.B. and G.I.M. are supported by the LIA-IRP CNRS Program (Apicolipid project).

AUTHOR CONTRIBUTIONS

S.A. and N.J.K. designed and performed experiments, analyzed and interpreted data, and wrote the manuscript. L.B. performed, analyzed, and interpreted data for EM. S.D. performed Nile red/LBPA and related IFAs. S.D. generated and analyzed the *Tg*DrpC-ΔPA mutant. C.S.A. generated and analyzed the double ACBP1-ACBP2- and ACBP1iKD/SCP2-KO mutants. M.J.S. helped perform and analyze the *P. falciparum* lipid starvation growth assay. C.B. helped perform *E. coli* complementation assays. B.T. performed and analyzed *T. gondii* proliferation assays and the related statistical analyses. G.I.M. supervised the *P. falciparum* lipid starvation growth assay. Y.Y.-B. performed, analyzed, interpreted, and supervised lipidomic analyses and wrote the manuscript. C.Y.B. led the project, designed and interpreted data, and wrote the manuscript.

DECLARATION OF INTERESTS

The authors declare no competing interests.

Received: March 22, 2019
Revised: November 12, 2019
Accepted: February 19, 2020
Published: March 17, 2020

REFERENCES

Adachi, Y., Itoh, K., Yamada, T., Cerveny, K.L., Suzuki, T.L., Macdonald, P., Frohman, M.A., Ramachandran, R., Iijima, M., and Sesaki, H. (2016). Coincident phosphatidic acid interaction restrains Drp1 in mitochondrial division. Mol. Cell *63*, 1034–1043.

Adachi, Y., Iijima, M., and Sesaki, H. (2018). An unstructured loop that is critical for interactions of the stalk domain of Drp1 with saturated phosphatidic acid. Small GTPases *9*, 472–479.

Amiar, S., MacRae, J.I., Callahan, D.L., Dubois, D., van Dooren, G.G., Shears, M.J., Cesbron-Delauw, M.-F., Maréchal, E., McConville, M.J., McFadden, G.I., et al. (2016). Apicoplast-localized lysophosphatidic acid precursor assembly is required for bulk phospholipid synthesis in toxoplasma gondii and relies on an algal/plant-like glycerol 3-phosphate acyltransferase. PLoS Pathog. *12*, e1005765.

Bisanz, C., Bastien, O., Grando, D., Jouhet, J., Maréchal, E., and Cesbron-Delauw, M.F. (2006). Toxoplasma gondii acyl-lipid metabolism: de novo synthesis from apicoplast-generated fatty acids versus scavenging of host cell precursors. Biochem. J. *394*, 197–205.

Botté, C.Y., Yamaryo-Botté, Y., Rupasinghe, T.W., Mullin, K.A., MacRae, J.I., Spurck, T.P., Kalanon, M., Shears, M.J., Coppel, R.L., Crellin, P.K., et al. (2013). Atypical lipid composition in the purified relict plastid (apicoplast) of malaria parasites. Proc. Natl. Acad. Sci. U S A *110*, 7506–7511.

Bougdour, A., Durandau, E., Brenier-Pinchart, M.-P., Ortet, P., Barakat, M., Kieffer, S., Curt-Varesano, A., Curt-Bertini, R.-L., Bastien, O., Coute, Y., Pelloux, H., and Hakimi, M.-A. (2013). Host cell subversion by Toxoplasma GRA16, an exported dense granule protein that targets the host cell nucleus and alters gene expression. Cell Host Microbe. *13*, 489–500.

Bougdour, A., Tardieux, I., and Hakimi, M.A. (2014). Toxoplasma exports dense granule proteins beyond the vacuole to the host cell nucleus and rewires the host genome expression. Cell. Microbiol. *16*, 334–343.

Braun, L., Brenier-Pinchart, M.-P., Hammoudi, P.-M., Cannella, D., Kieffer-Jaquinod, S., Vollaire, J., Josserand, V., Touquet, B., Couté, Y., Tardieux, I., Bougdour, A., and Hakimi, M.-A. (2019). The Toxoplasma effector TEEGR promotes parasite persistence by modulating NF-κB signalling via EZH2. Nat. Microbiol. *4*, 1208–1220.

Breinich, M.S., Ferguson, D.J., Foth, B.J., van Dooren, G.G., Lebrun, M., Quon, D.V., Striepen, B., Bradley, P.J., Frischknecht, F., Carruthers, V.B., and Meissner, M. (2009). A dynamin is required for the biogenesis of secretory organelles in Toxoplasma gondii. Curr. Biol. *19*, 277–286.

Brown, W.J., Plutner, H., Drecktrah, D., Judson, B.L., and Balch, W.E. (2008). The lysophospholipid acyltransferase antagonist CI-976 inhibits a late step in COPII vesicle budding. Traffic *9*, 786–797.

Burger, K.N.J., Demel, R.A., Schmid, S.L., and de Kruijff, B. (2000). Dynamin is membrane-active: lipid insertion is induced by phosphoinositides and phosphatidic acid. Biochemistry *39*, 12485–12493.

Chen, N., LaCrue, A.N., Teuscher, F., Waters, N.C., Gatton, M.L., Kyle, D.E., and Cheng, Q. (2014). Fatty acid synthesis and pyruvate metabolism pathways remain active in dihydroartemisinin-induced dormant ring stages of Plasmodium falciparum. Antimicrob Agents Chemother *58*, 4773–4781.

Coleman, J. (1990). Characterization of Escherichia coli cells deficient in 1-acyl-sn-glycerol-3- phosphate acyltransferase activity. J. Biol. Chem. *265*, 17215–17221.

Costa, G., Gildenhard, M., Eldering, M., Lindquist, R.L., Hauser, A.E., Sauerwein, R., Goosmann, C., Brinkmann, V., Carrillo-Bustamante, P., and Levashina, E.A. (2018). Non-competitive resource exploitation within mosquito shapes within-host malaria infectivity and virulence. Nat. Commun. *9*, 3474.

Curt-Varesano, A., Braun, L., Ranquet, C., Hakimi, M.-A., and Bougdour, A. (2016). The aspartyl protease TgASP5 mediates the export of the Toxoplasma GRA16 and GRA24 effectors into host cells. Cell. Microbiol. *18*, 151–167.

Daily, J.P., Scanfeld, D., Pochet, N., Le Roch, K., Plouffe, D., Kamal, M., Sarr, O., Mboup, S., Ndir, O., Wypij, D., et al. (2007). Distinct physiological states of Plasmodium falciparum in malaria-infected patients. Nature *450*, 1091–1095.

Dereeper, A., Guignon, V., Blanc, G., Audic, S., Buffet, S., Chevenet, F., Dufayard, J.-F., Guindon, S., Lefort, V., Lescot, M., et al. (2008). Phylogeny.fr: robust phylogenetic analysis for the non-specialist. Nucleic Acids Res. *36*, W465–W469.

Dubois, D., Fernandes, S., Amiar, S., Dass, S., Katris, N.J., Botté, C.Y., and Yamaryo-Botté, Y. (2018). *Toxoplasma gondii* acetyl-CoA synthetase is involved in fatty acid elongation (of long fatty acid chains) during tachyzoite life stages. J. Lipid Res. *59*, 994–1004.

Franco, M., Panas, M.W., Marino, N.D., Lee, M.C., Buchholz, K.R., Kelly, F.D., Bednarski, J.J., Sleckman, B.P., Pourmand, N., and Boothroyd, J.C. (2016). A novel secreted protein, MYR1, is central to Toxoplasma's manipulation of host cells. MBio *7*, e02231-15.

Gras, S., Jimenez-Ruiz, E., Klinger, C.M., Schneider, K., Klingl, A., Lemgruber, L., and Meissner, M. (2019). An endocytic-secretory cycle participates in Toxoplasma gondii in motility. PLoS Biol. *17*, e3000060.

Guindon, S., Dufayard, J.F., Lefort, V., Anisimova, M., Hordijk, W., and Gascuel, O. (2010). New algorithms and methods to estimate maximum-likelihood phylogenies: assessing the performance of PhyML 3.0. Syst. Biol. *59*, 307–321.

Gulati, S., Ekland, E.H., Ruggles, K.V., Chan, R.B., Jayabalasingham, B., Zhou, B., Mantel, P.Y., Lee, M.C., Spottiswoode, N., Coburn-Flynn, O., et al. (2015). Profiling the Essential nature of lipid metabolism in asexual blood and gametocyte stages of Plasmodium falciparum. Cell Host Microbe *18*, 371–381.

Heredero-Bermejo, I., Varberg, J.M., Charvat, R., Jacobs, K., Garbuz, T., Sullivan, W.J., Jr., and Arrizabalaga, G. (2019). TgDrpC, an atypical dynamin-related protein in Toxoplasma gondii, is associated with vesicular transport factors and parasite division. Mol. Microbiol. *111*, 46–64.

Hu, X., Binns, D., and Reese, M.L. (2017). The coccidian parasites *Toxoplasma* and *Neospora* dysregulate mammalian lipid droplet biogenesis. J. Biol. Chem. *292*, 11009–11020.

Huynh, M.H., and Carruthers, V.B. (2009). Tagging of endogenous genes in a Toxoplasma gondii strain lacking Ku80. Eukaryot. Cell *8*, 530–539.

Janouskovec, J., Horák, A., Oborník, M., Lukeš, J., and Keeling, P.J. (2010). A common red algal origin of the apicomplexan, dinoflagellate, and heterokont plastids. Proc. Natl. Acad. Sci. U S A *107*, 10949–10954.

Katris, N.J., van Dooren, G.G., McMillan, P.J., Hanssen, E., Tilley, L., and Waller, R.F. (2014). The apical complex provides a regulated gateway for secretion of invasion factors in Toxoplasma. PLoS Pathog. *10*, e1004074.

Kim, K., Soldati, D., and Boothroyd, J.C. (1993). Gene replacement in Toxoplasma gondii with chloramphenicol acetyltransferase as selectable marker. Science *262*, 911–914.

Kobayashi, T., Stang, E., Fang, K.S., de Moerloose, P., Parton, R.G., and Gruenberg, J. (1998). A lipid associated with the antiphospholipid syndrome regulates endosome structure and function. Nature *392*, 193–197.

Kooijman, E.E., Chupin, V., Fuller, N.L., Kozlov, M.M., de Kruijff, B., Burger, K.N.J., and Rand, P.R. (2005). Spontaneous curvature of phosphatidic acid and lysophosphatidic acid. Biochemistry *44*, 2097–2102.

Larkin, M.A., Blackshields, G., Brown, N.P., Chenna, R., McGettigan, P.A., McWilliam, H., Valentin, F., Wallace, I.M., Wilm, A., Lopez, R., et al. (2007). Clustal W and Clustal X version 2.0. Bioinformatics *23*, 2947–2948.

Li, W., Cowley, A., Uludag, M., Gur, T., McWilliam, H., Squizzato, S., Park, Y.M., Buso, N., and Lopez, R. (2015). The EMBL-EBI bioinformatics web and programmatic tools framework. Nucleic Acids Res. *43* (*W1*), W580–W584.

MacRae, J.I., Maréchal, E., Biot, C., and Botté, C.Y. (2012). The apicoplast: a key target to cure malaria. Curr. Pharm. Des. *18*, 3490–3504.

Mancio-Silva, L., Slavic, K., Grilo Ruivo, M.T., Grosso, A.R., Modrzynska, K.K., Vera, I.M., Sales-Dias, J., Gomes, A.R., MacPherson, C.R., Crozet, P., et al. (2017). Nutrient sensing modulates malaria parasite virulence. Nature *547*, 213–216.

Martins-Duarte, E.S., Dubar, F., Lawton, P., da Silva, C.F., Soeiro, Mde.N., de Souza, W., Biot, C., and Vommaro, R.C. (2015). Ciprofloxacin derivatives affect parasite cell division and increase the survival of mice infected with Toxoplasma gondii. PLoS ONE *10*, e0125705.

Mazumdar, J., H Wilson, E., Masek, K., A Hunter, C., and Striepen, B. (2006). Apicoplast fatty acid synthesis is essential for organelle biogenesis and parasite survival in Toxoplasma gondii. Proc. Natl. Acad. Sci. U S A *103*, 13192–13197.

Melatti, C., Pieperhoff, M., Lemgruber, L., Pohl, E., Sheiner, L., and Meissner, M. (2019). A unique dynamin-related protein is essential for mitochondrial fission in Toxoplasma gondii. PLoS Pathog. *15*, e1007512.

Menard, D., and Dondorp, A. (2017). Antimalarial drug resistance: a threat to malaria elimination. Cold Spring Harb. Perspect. Med. *7*, a025619.

Mi-Ichi, F., Kita, K., and Mitamura, T. (2006). Intraerythrocytic Plasmodium falciparum utilize a broad range of serum-derived fatty acids with limited modification for their growth. Parasitology *133*, 399–410.

Mi-Ichi, F., Kano, S., and Mitamura, T. (2007). Oleic acid is indispensable for intraerythrocytic proliferation of *Plasmodium falciparum*. Parasitology *134*, 1671–1677.

Mitamura, T., Hanada, K., Ko-Mitamura, E.P., Nishijima, M., and Horii, T. (2000). Serum factors governing intraerythrocytic development and cell cycle progression of Plasmodium falciparum. Parasitol. Int. *49*, 219–229.

Mueller, C., Klages, N., Jacot, D., Santos, J.M., Cabrera, A., Gilberger, T.W., Dubremetz, J.-F., and Soldati-Favre, D. (2013). The Toxoplasma protein ARO mediates the apical positioning of rhoptry organelles, a prerequisite for host cell invasion. Cell Host Microbe *13*, 289–301.

Nolan, S.J., Romano, J.D., and Coppens, I. (2017). Host lipid droplets: an important source of lipids salvaged by the intracellular parasite Toxoplasma gondii. PLoS Pathog. *13*, e1006362.

Ohlrogge, J., and Browse, J. (1995). Lipid biosynthesis. Plant Cell *7*, 957–970.

Pernas, L., Adomako-Ankomah, Y., Shastri, A.J., Ewald, S.E., Treeck, M., Boyle, J.P., and Boothroyd, J.C. (2014). Toxoplasma effector MAF1 mediates recruitment of host mitochondria and impacts the host response. PLoS Biol. *12*, e1001845.

Ramakrishnan, S., Docampo, M.D., Macrae, J.I., Pujol, F.M., Brooks, C.F., van Dooren, G.G., Hiltunen, J.K., Kastaniotis, A.J., McConville, M.J., and Striepen, B. (2012). Apicoplast and endoplasmic reticulum cooperate in fatty acid biosynthesis in apicomplexan parasite *Toxoplasma gondii*. J. Biol. Chem. *287*, 4957–4971.

Romano, J.D., Nolan, S.J., Porter, C., Ehrenman, K., Hartman, E.J., Hsia, R.C., and Coppens, I. (2017). The parasite *Toxoplasma* sequesters diverse Rab host vesicles within an intravacuolar network. J. Cell Biol. *216*, 4235–4254.

Schmidt, A., Wolde, M., Thiele, C., Fest, W., Kratzin, H., Podtelejnikov, A.V., Witke, W., Huttner, W.B., and Söling, H.D. (1999). Endophilin I mediates synaptic vesicle formation by transfer of arachidonate to lysophosphatidic acid. Nature *401*, 133–141.

Shears, M.J., MacRae, J.I., Mollard, V., Goodman, C.D., Sturm, A., Orchard, L.M., Llinás, M., McConville, M.J., Botté, C.Y., and McFadden, G.I. (2017). Characterization of the Plasmodium falciparum and P. berghei glycerol 3-phosphate acyltransferase involved in FASII fatty acid utilization in the malaria parasite apicoplast. Cell. Microbiol. *19*.

Sheiner, L., Demerly, J.L., Poulsen, N., Beatty, W.L., Lucas, O., Behnke, M.S., White, M.W., and Striepen, B. (2011). A systematic screen to discover and analyze apicoplast proteins identifies a conserved and essential protein import factor. PLoS Pathog. *7*, e1002392.

Shin, J.J.H., and Loewen, C.J.R. (2011). Putting the pH into phosphatidic acid signaling. BMC Biol. *9*, 85.

Sidik, S.M., Hackett, C.G., Tran, F., Westwood, N.J., and Lourido, S. (2014). Efficient genome engineering of Toxoplasma gondii using CRISPR/Cas9. PLoS ONE *9*, e100450.

Sidik, S.M., Huet, D., Ganesan, S.M., Huynh, M.H., Wang, T., Nasamu, A.S., Thiru, P., Saeij, J.P.J., Carruthers, V.B., Niles, J.C., and Lourido, S. (2016). A genome-wide CRISPR screen in Toxoplasma identifies essential apicomplexan genes. Cell *166*, 1423–1435.e12.

Trager, W., and Jensen, J.B. (1976). Human malaria parasites in continuous culture. Science *196*, 673–675.

Uboldi, A.D., Wilde, M.-L., McRae, E.A., Stewart, R.J., Dagley, L.F., Yang, L., Katris, N.J., Hapuarachchi, S.V., Coffey, M.J., Lehane, A.M., Botte, C.Y., Waller, R.F., Webb, A.I., McConville, M.J., and Tonkin, C.J. (2018). Protein kinase A negatively regulates Ca^{2+} signalling in *Toxoplasma gondii*. PLOS Biology *16*, e2005642.

van Dooren, G.G., Reiff, S.B., Tomova, C., Meissner, M., Humbel, B.M., and Striepen, B. (2009). A novel dynamin-related protein has been recruited for apicoplast fission in Toxoplasma gondii. Curr. Biol. *19*, 267–276.

Vaughan, A.M., O'Neill, M.T., Tarun, A.S., Camargo, N., Phuong, T.M., Aly, A.S., Cowman, A.F., and Kappe, S.H. (2009). Type II fatty acid synthesis is essential only for malaria parasite late liver stage development. Cell. Microbiol. *11*, 506–520.

Waller, R.F., Keeling, P.J., Donald, R.G., Striepen, B., Handman, E., Lang-Unnasch, N., Cowman, A.F., Besra, G.S., Roos, D.S., and McFadden, G.I. (1998). Nuclear-encoded proteins target to the plastid in *Toxoplasma gondii* and *Plasmodium falciparum*. Proc. Natl. Acad. Sci. U S A *95*, 12352–12357.

Welti, R., Mui, E., Sparks, A., Wernimont, S., Isaac, G., Kirisits, M., Roth, M., Roberts, C.W., Botté, C., Maréchal, E., and McLeod, R. (2007). Lipidomic analysis of Toxoplasma gondii reveals unusual polar lipids. Biochemistry *46*, 13882–13890.

Yeh, E., and DeRisi, J.L. (2011). Chemical rescue of malaria parasites lacking an apicoplast defines organelle function in blood-stage Plasmodium falciparum. PLoS Biol. *9*, e1001138.

Ylä-Anttila, P., Vihinen, H., Jokitalo, E., and Eskelinen, E.L. (2009). Monitoring autophagy by electron microscopy in mammalian cells. Methods Enzymol. *452*, 143–164.

Yu, M., Kumar, T.R., Nkrumah, L.J., Coppi, A., Retzlaff, S., Li, C.D., Kelly, B.J., Moura, P.A., Lakshmanan, V., Freundlich, J.S., et al. (2008). The fatty acid biosynthesis enzyme FabI plays a key role in the development of liver-stage malarial parasites. Cell Host Microbe *4*, 567–578.

Zhang, M., Wang, C., Otto, T.D., Oberstaller, J., Liao, X., Adapa, S.R., Udenze, K., Bronner, I.F., Casandra, D., Mayho, M., et al. (2018). Uncovering the essential genes of the human malaria parasite *Plasmodium falciparum* by saturation mutagenesis. Science *360*, eaap7847.

Zuzarte-Luís, V., Mello-Vieira, J., Marreiros, I.M., Liehl, P., Chora, A.F., Carret, C.K., Carvalho, T., and Mota, M.M. (2017). Dietary alterations modulate susceptibility to Plasmodium infection. Nat. Microbiol. *2*, 1600–1607.

STAR★METHODS

KEY RESOURCES TABLE

REAGENT or RESOURCE	SOURCE	IDENTIFIER
Antibodies		
Mouse anti-HA	Roche	Cat#: 11867423001; RRID:AB_390918
anti-CPN60	Boris Striepen	N/A
anti-LBPA	Echelon Biosciences	Cat#: 117Z-PLBPA-50ug
Mouse anti-Sag1	Abcam	N/A
Anti-LC3B antibody produced in rabbit	Sigma	Cat#: L7543; RRID:AB_796155
Rabbit anti-TOM40	Giel van Dooren	N/A
rabbit anti-GAP45	Dominique Soldati Lab	N/A
rabbit polyclonal anti-IMC1	Gary Ward Lab	N/A
Anti-MIC2	David Sibley	N/A
Anti-GRA1	Cesbron-Delauw Lab	N/A
Rabbit anti-ACP	McFadden lab	N/A
Rabbit polyclonal anti-MIC4	Dominique Soldati Lab	N/A
rabbit anti-Sumo21	Hakimi lab	N/A
Goat a Mouse Alexa 488	ThermoFisher Scientific	Cat#: A11001; RRID:AB_2534069
Goat a Rb Alexa 546	ThermoFisher Scientific	Cat#: A11003; RRID:AB_141370
Goat a Mouse Alexa 546	ThermoFisher Scientific	Cat#: A11010; RRID:AB_2534077
Goat a Rb Alexa 488	ThermoFisher Scientific	Cat#: A11008; RRID:AB_143165
Bacterial and Virus Strains		
E. coli SM2-1 ΔplsC	Coleman, 1990	Coli Genetic Stock Center #7587, Yale University
Biological Samples		
Red Blood Cells	Etablissement francais du sang (EFS)	N/A
Chemicals, Peptides, and Recombinant Proteins		
DMEM, High Glucose	GIBCO, ThermoFisher Scientific	Cat#: 41965-062
DMEM, no Glucose	GIBCO, ThermoFisher Scientific	Cat#: 11966-025
RPMI 1640 Medium, HEPES	GIBCO, ThermoFisher Scientific	Cat#: 52400-025
Fetal Calf Serum, Sourced from South America (EU Approved).	ThermoFisher Scientific	Cat#: 10270-106
AlbuMAX® II	ThermoFisher Scientific	Cat#: 11021-045
GLUCOSE-D U-13C6 99%13C 10 g	Cambridge Isotope Laboratories (Eurisotop)	Cat#: CLM-1396-10
Sorbitol	Sigma	Cat#: S1876
Giemsa's azur eosin methylene blue solution	Merck	Cat#: MEF1092040500
fatty acid free bovine serum albumin	Sigma	Cat#: A8806
palmitic acid (C16:0)	Sigma	Cat#: P0500-10G
oleic acid (C18:1)	Sigma	Cat#: 75090-5ML
tridecanoic acid (C13:0)	Sigma	Cat#: 91988-5G
pentadecanoic acid C15:0	Sigma	Cat#: P6125-1G
MethPrep II (Alltech)	Alltech	Grace 5122149
HCl	Sigma	Cat#: 258148
1-butanol	Sigma	N/A
Chloroform	Sigma	Cat#: 34854
Hexane	Sigma	Cat#: 34484
Methanol	Sigma	Cat#: 34860

(*Continued on next page*)

Continued

REAGENT or RESOURCE	SOURCE	IDENTIFIER
Acetone	Sigma	Cat#: 34850
Ammonium hydroxie	Sigma	Cat#: 221228
Acetic acid	Sigma	Cat#: 27221
Fluorescent NBD PA18:1, 12:0	Avanti Polar Lipids	Cat#: 810176P-1mg
Fluorescent NBD PC 18:1, 12:0	Avanti Polar Lipids	Cat#: 810133P-1mg
PA 18:1, 16:0	Avanti Polar Lipids	Cat#: 840857
PA 14:0, 14:0	Avanti Polar Lipids	Cat#: 830845
PA(C17:0/C17:0)	Avanti Polar lipids	Cat#: 830856
HPTLC60	Merck	Cat#: MEF1056330001
Nile red	Sigma	Cat#: 72485
Chloramphenicol	Sigma	Cat#: C0378-5G
Pyrimethamine	Sigma	Cat#: 46706
Mycophenolic acid	Sigma	Cat#: M3536
Xanthine	Sigma	Cat#: X3627
Fluoro-Gel, (with Tris Buffer)	Electron Micrsoscopy Sciences	Cat#: 17985-10
0.1 M cacodylate buffer	Electron Micrsoscopy Sciences	Cat#: 11650
25% glutaraldehyde	Electron Microscopy Sciences	Cat#: 16220
4% osmium tetroxide	Electron Micrsoscopy Sciences	Cat#: 19150?
uranyl acetate	Electron Micrsoscopy Sciences	Cat#: 22400
Epon812	Electron Micrsoscopy Sciences	Cat#: 13940
Crystal Violet	Sigma	Cat#: C0775
Hoechst 33342	ThermoFisher Scientific	Cat#: 1015-0888
A23187	Sigma	Cat#: C7522
DIMETHYL SULFOXIDE,	Sigma	Cat#: D2438
16% Paraformaldehyde	Electron Microscopy Sciences	Cat#: 15710
Triton X-100	Sigma	Cat#: T9284-100ML
K_2SO_4	Sigma	Cat#: 60528
$MgSO_4$	Sigma	Cat#: M2643
sucrose	Sigma	Cat#: 84100
glucose	Sigma	Cat#: G5400
Tris	Dutscher	Cat#: 091572
BSA	Sigma	Cat#: A9418
HEPES	Sigma	Cat#: H4034
DAPI	Sigma	Cat #: D9542
Critical Commercial Assays		
NucleoSpin Gel and PCR Clean-up	Macherey-Nagel	Cat #: 740609
NucleoSpin Plasmid	Macherey-Nagel	Cat #: 740588
NucleoBond Xtra Midi	Macherey-Nagel	Cat #: 740410
Nucleo spin RNA II	Macherey-Nagel	Cat #: 740955
DNA sequencing	Eurofins Genomics	N/A
Oligo nucleotide synthesis	Sigma	N/A
Q5® Site-Directed Mutagenesis Kit	NEB	Cat#: E0554S
Experimental Models: Cell Lines		
Human Foreskin fibroblasts	ATCC® CCL-171	N/A
Experimental Models: Organisms/Strains		
T. gondii RH TATi1-*ΔKu80*	Sheiner et al., 2011	N/A
T. gondii RHΔKu80	Huynh and Carruthers, 2009	N/A
T. gondii PRU Type II	Marie-France Cesbron Delauw	N/A

(*Continued on next page*)

Continued

REAGENT or RESOURCE	SOURCE	IDENTIFIER
T. gondii ME49 Type II	Jeroen Saeij	N/A
T. gondii ASPV KO	Curt-Varesano et al., 2016	N/A
T. gondii MYR1 KO	Braun et al., 2019	N/A
T. gondii ACASiKD	Dubois et al., 2018	N/A
T. gondii ARO-iKD	Mueller et al., 2013	N/A
T. gondii PKA-iKD	Uboldi et al., 2018	N/A
T. gondii GRA16	Bougdour et al., 2013	N/A
T. gondii ATS1	Amiar et al., 2016	N/A
P. falciparum PfFabI KO	Vaughan et al., 2009	N/A
P. falciparum NF54	Walter and Eliza Hall Institute	N/A
T. gondii ACBP1 iKD	This study	N/A
T. gondii ACBP2 iKD	This study	N/A
T. gondii ACBP1/ACBP3 double KO	This study	N/A
T. gondii ACBP1/SCP2 double KO	This study	N/A
T. gondii ATS2-HA	This study	N/A
T. gondii ATS2-KI	This study	N/A
T. gondii ATS2-KO	This study	N/A
Oligonucleotides		
All primers outlined in materials and methods section.		N/A
Recombinant DNA		
U6-Unversal Plasmid	Sidik et al., 2014 (Addgene)	N/A
Cas9-RFP plasmid	Dominique Soldati	N/A
pTOXO_Cas9-CRISPR	Hakimi Lab, Grenoble, France	N/A
pTOXO_Cas9-CRISPR::g*Tg*ATS2-KI	This study	N/A
pTOXO_Cas9-CRISPR::g*Tg*ATS2-KO	This study	N/A
pTOXO_Cas9-CRISPR::g*Tg*AGPAT-KO	This study	N/A
graCAT-sagMcherry	This study	N/A
pLIC HA3 DHFR	Huynh and Carruthers, 2009	N/A
pLIC HA3 CAT	Sheiner et al., 2011	N/A
ATS2 KO plasmid MAH	This Study	N/A
pPR2 HA3 DHFR	Katris et al., 2014	N/A
graCAT sagmCherry KO plasmid	This study	N/A
Morn1-myc	Marc-Jan Gubbels	N/A
pLIC-*Tg*ATS2-3HA-DHFR	This study	N/A
pLIC-*Tg*AGPAT-3HA-DHFR	This study	N/A
pMORN1-CherryRFP-MORN1/SagCAT	This study	N/A
pQE30Xa vector	Quiagen	33203
Software and Algorithms		
Prism software	GraphPad	N/A
ImageJ	NIH	N/A
Mass Hunter Quantification software	Agilent	N/A
Other		
Gas chromatography-mass spectrometry	Agilent	5977A-7890B

MATERIALS AND METHODS

See STAR Methods **KEY RESOURCES** Table

LEAD CONTACT AND MATERIALS AVAILABILITY

Materials generated in this study are available upon request. Information and requests for resources and reagents should be directed to the Lead Contact, Cyrille Botte (cyrille.botte@univ-grenoble-alpes.fr). Plasmids and parasite lines generated in this study will be made freely available by the Lead Contact upon request which may require the completion of a Material Transfer Agreement.

EXPERIMENTAL MODEL AND SUBJECT DETAILS

T. gondii culture

Toxoplasma gondii parental lines RH TATi1-ΔKu80 (Sheiner et al., 2011) and RH-ΔKu80 (Huynh and Carruthers, 2009) and derived transgenic cell lines were grown in confluent human foreskin fibroblasts (HFFs) in high glucose DMEM supplemented with 1% Foetal Bovine Serum, as described (Amiar et al., 2016). ME49 parental cell cultures were additionally supplemented with 10 mM HEPES.

P. falciparum culture

P. falciparum NF54 wild-type parasites were maintained as previously described (Trager and Jensen, 1976). Briefly, *Plasmodium* blood stage parasites were maintained at 2% hematocrit in 1640 RPMI-HEPES supplemented with 10% AlbuMAX II (GIBCO) and 0.25% gentamycin. Parasites were grown sealed Perspex chambers gassed with beta mix gas (1%O_2 5%CO_2, 94% N_2) at 37°C and maintained on 48-hour cycles.

METHOD DETAILS

Gene identification and sequence analysis
T.gondii plasmid constructs
T.gondii transfection
T.gondii growth assays
T.gondii Red/Green parasite invasion assay:
Plasmodium falciparum growth assays:
Immunofluorescence assay and Microscopy
Nile red staining of lipid droplets
Activity analysis in LPAAT-deficient *E. coli* strains
Transmission electron microscopy:
Lipidomic analysis by GCMS extraction from *T. gondii* tachyzoites
Stable isotope labeling of *T. gondii*
Phospholipid import assay:
Quantification and statistical analysis

Gene identification and sequence analysis

Arabidopsis thaliana sequence of ATS2 (GenBankTM and TAIRTM IDs: NP_194787 and AT4G30580 respectively) was used as a query sequences for BLAST searches against the Toxoplasma gondii genome on ToxoDB database (https://www.toxodb.org/). Phylogenetic analysis of AGPAT related proteins was performed on the Phylogeny.fr platform (Dereeper et al., 2008). Protein sequences were then aligned by ClustalW software (Larkin et al., 2007) and the maximum likelihood phylogeny was generated using the PhyML (Guindon et al., 2010). We generated multiple sequence alignment using Clustal Omega (Li et al., 2015).

T. gondii plasmid constructs

Plasmid LIC-3HA-DHFR was used to generate a 3′ endogenous tagging with 3xHA coding sequence of ToxoDB: TGME49_297640 (*Tg*ATS2) and ToxoDB: TGME49_240860 (*Tg*AGPAT). A 2229 bp fragment corresponding to the 3′ of TgATS2 was amplified from genomic DNA using primer sets 5′-TCCTCCACTTCCAATTTTAGCGTTCGTCTCGGTGGCGGC-3′ and 5′-TACTTCCAATC CAATGCTTCAGACACTCGGTGCAAA-3. A 5466 bp fragment corresponding to promoter and gene sequence of TgAGPAT was amplified using primer sets 5′-TACTTCCAATCCAATGCAGCCAGCAAAGGACGAAAGG-3′ and 5′-TCCTCCACTTCCAATTTTAGC GAGACCGTGGCCTCGGTGGG-3′. These fragments were cloned into pLIC-3HA-DHFR vector as described previously (Huynh and Carruthers, 2009). Vectors LIC-TgATS2-3HA-DHFR and LIC-TgAGPAT-3HA-DHFR were confirmed by PCR screen using primer sets 5′-GCATAATCGGGCACATCATA-3′ and 5′-ATACGCATAATCGGGCACATCATA-3′and by sequencing (Eurofin genomicsTM).

Plasmid pTOXO_Cas9-CRISPR (gift from Hakimi Lab, Grenoble, France) was used to integrate a gRNA within BsaI restriction site as previously described (Sidik et al., 2014). Briefly, Crisp-Fwd and Crisp-Rv primer sets were phosphorylated and annealed: *Tg*ATS2-KI: 5′-AAGTTACGGGTGTGCGCCGCCTTGCG-3′ and 5′-AAAACGCAAGGCGGCGCACACCCGTA-3′, *Tg*ATS2-KO: 5′-AAGTTG GAGCGCCGACGGGCGACTGG-3′ and 5′-AAAACCAGTCGCCCGTCGGCGCTCCA-3′, *Tg*AGPAT-KO: 5′-AAGTTCTCTGCCGAGT TCCAATCGCG-3′ and 5′-AAAACGCGATTGGAACTCGGCAGAGA-3′. The gRNAs were then ligated into pTOXO_Cas9-CRISPR plasmid linearized with BsaI, yielding pTOXO_Cas9-CRISPR::gTgATS2-KI, pTOXO_Cas9-CRISPR::gTgATS2-KO and pTOXO_Cas9-CRISPR::gTgAGPAT-KO, respectively.

For *Tg*ATS2 knockout by CRISPR-CAs9, an appropriate HXGPRT cassette amplified by PCR from pMini (kind gift from the Hakimi laboratory) using those primer sets, TgATS2-KI: 5′-GAGGCCCTGCGTCTCCTCAAGCG- AAAGGCGCCGCCACAGTCGACGGGTGT GCGCC-GCCTCAGCACGAAACCT-TGCATTCAAACC-3′ and 5′-GCTACTCCTTCTTCCCCTCTCG- CGTTGTGTGTCTCCCCGTCG CGTTCTGCGTCGCCAGCAGTGTCACTGTAGCCTGCCAGAACA-3′; *Tg*ATS2-KO: 5′-GACACACAACGCGAGAGGGGAAGAAGGA GTAGCTCTCG-TCGCCTTTCCAGAAGGTACTCCAGCACGAAACCTTGCATTCAAACC −3′ and 5′-CTTCG- CTGCTCGTTCGTCTTC ATGTGGGGAAGGAGCAGCACGAAACCTTG- CATTCAAACC-3′.

DrpA and DrpC were localized by CRISPR Cas9 strategy. Guides were inserted into Cas9 U6 universal plasmid (Sidik et al., 2014) by either standard ligation of annealed primers or Q5 mutagenesis. Cells were transfected together with PCR product encoding either HA3-CAT and DrpC homology flanks, for DrpC or GFP sequence without selection and DrpA homology flanks for DrpA.

For DrpC HA3 CAT CRISPR Cas9 tagging, DrpC was tagged at the 3′ terminus by CRISPR Cas9 (Sidik et al., 2014). For DrpC, the protospacer gaatggggcttgaaactgtg was chosen and primers 5′ AAGTTgaatggggcttgaaactgtgG 3′ and 5′ AAAACcacagtttcaagccc cattcA 3′ were annealed together and ligated into U6 universal plasmid (Sidik et al., 2014). The HA3-CAT cassette was PCR amplified by primers with 50 bp homology flanks (FOR aggaagttccggtcggcttccgtcaccgtt- gaatggggctAAAATTGGAAGTGGAGGACGGG and REV gttcttcccagtgctctggcga- agtgggccagcacaagccaGTTGTAAAACGACGGCCAGTG) and overhang corresponding to the 3′ end of DrpC and in frame with HAx3. 50 μg of both plasmid and PCR product were transfected and placed under chloramphenicol selection (Kim et al., 1993). DrpC was also localized by pLIC-HA3-CAT using primers TACTTCCAATCCAATTTAGCgcacggtctgttgttc tacg and TCCTCCACTTCCAATTTTAGCagccccattcaacggtg (Sheiner et al., 2011). For DrpA, the protospacer gatggaggagttgattcctg was inserted into the Universal Cas9 Plasmid using the NEB Q5 site directed mutagenesis Kit with the oligos 5′ gatggaggagtt gattcctgGTTTTAGAGCTAGAAATAGC 3′ and 5′ AACTTGACATCCCCATTTAC 3′. PCR product was amplified using 5′- gttgccctggctt cctcctctttctctcctctctctcaagATGGCGGTGAGCAAGGGC3′ 5′- cgtcctgcaggcgattgacAacaggaatcaactcctccatCCCGGGCTTGTA CAGC 3′ using GFP cDNA as a template and co-transfected with U6 guide RNA plasmid described above. Transfected parasites were seeded onto coverslips and then transiently observed after 24 hours growth.

For the DrpC PA domain mutation, a guide was identified within a DrpC exon and the 20 bp protospacer (5′ ggcgagctgatcctcgag gt 3′) was inserted into a CRISPR Cas9 plasmid using Q5 with primers 5′ ggcgagctgatcctcgaggt-GTTTTAGAGCTAGAAATAGCA AG 3′ and 5′ AACTTGACATCCCCATTTAC 3′ (Sidik et al., 2014). The PCR product was amplified with the following primers 5′ cgtcgccttgtacggaaacgctt-ggagacgcaaaaacggattGCGGTGAGCAAGGGCG 3′ and 5′ agccccattcaacggtgacggaagccgaccggaacttcc tgcCCCGGGCTTGTACAGC 3′. The guide and the PCR product were transfected together and parasites were seeded onto HFFs on coverslips and grown for 24 h. Cells were labeled with anti-IMC and anti-HA antibodies and viewed under the microscope. Cas9 expression was visualized by the Cas9-RFP tag to observe parasites with DrpC-HA normally (Cas9-RFP absent) or with the PA binding domain disrupted (Cas9-RFP present).

For TgACBP1i-HA KD, the 5′ UTR flank was PCR amplified using primers ACACGGGCCCACGATCAGTTGAGTTCCGAGG and GACACATATGAAGG -TCGAAAGAAGGCTCC and inserted into ApaI/NdeI sites of pPR2-HA3 (Katris et al., 2014). The 3′ flank was amplified using primers CTTGCCCGGGATGGCCTCGCgtaaggaagg and CAGAGCGGCCGCCTGT -GTCGTGAGCGAGTGAC and then inserted in frame with a Tet7O/SAG4 promoter using XmaI/NotI sites. Plasmid was linearized with NotI prior to transfection and selected using pyrimethamine. For ACBP2, flanks were PCR amplified using respective primers below into the plasmid pPR2-GFP or pPR2-mCherry (adapted from pPR2-HA3, (Katris et al., 2014). The 5′ UTR flank was amplified using CTGAGGGCCCGC GACGCTCCAGAAGACTCC and GTACCATA -TGTTATTATATGGTTGAAAGAAGC inserted first using ApaI/NdeI sites. Next, the 3′ UTR flank was amplified using GACTGATATCGATT -ACGGCTTCAACTCCGTC and ATTAGCGGCCGCCTTCATAGGAC -CAGAGCC and inserted using MscI/NotI sites. ACBP2 cDNA sequence was amplified using GATCAGATCTAAAATGGCGAGGCCTGTA CATCTTGGG and GTACCCTAGGAGTAGCTTTTGAGGCGGTG inserted last into BglII/AvrII sites then selected using pyrimethamine. ACBP1 pLIC was PCR amplified using pLIC primers TACTTCCAATCCAATTTAGCTACAACGGAGCAGACAGAGG and TCCTCCACTTCCAATTTTAGCCGCGCTTTTCTCGCGCC into pLIC-HA3-CAT (Sheiner et al., 2011), and linearized prior to transfection and selection on chloramphenicol.

For ACBP1 KO/ACBP2iKD the following protospacer was selected, 5′ GGGGCGTTCCACTGAGAGAA 3′, inserted into a U6-Cas9 expression construct (Sidik et al., 2014). A PCR product w homology flanks for ACBP1 was made with the following primers 5′ ATTTTTTCCAAAGTCCATGCTGGGTTTCTCCCCTG-TGTCTAGGGAGCCTTAAAACCCTCGAAGGCTGCTAGTAC 3′ and

5′ AGATGATTTGACGACACGCGCCTCGGAAGTCGCTCTGTTTACG- CGCTTTTTGCCAGAACACTTGTCAACCG3′ using a graCAT-sag-mcherry resistance cassette as a template and transfected with U6 construct and selected for with Chloramphenicol. For SCP2 KO/ACBP1iKD, the following protospacer5′ GTACGCTTGCTGTGGAAAAA 3′ was inserted into a U6-Cas9 construct and co-transfected with the following primers 5′

gaacaggtgctgacacttgctcgagaatcctgtcgctgcaagttctgagttAAAACCCTCGAAGGCTGCTAGTAC 3′ and 5′ agggcgagtttcacgaaatc ttcgt -ccaacaaagtgatggtgcagtcgcaTGCCAGAACACTTGTCAACCG 3′ using a graCAT-sag-mcherry resistance cassette and selected for with chloramphenicol.

T. gondii transfection

RH-ΔKu80 parasite line was transfected with 100 μg of pLIC-TgATS2-3HA-DHFR linearized with BlpI for stable integration of HA-tag at C terminus of TgATS2. 150 μg pTOXO_Cas9-CRISPR::gTgATS2-KO and pTOXO_Cas9-CRISPR::gTgAGPAT-KO were transfected in TgATS2-HA line with 10 μg of appropriate HXGPRT cassette for *Tg*ATS2-KI and *Tg*ATS2-KO, PCR product as described above. Electroporations were performed in a 2-mm cuvette in a BTX ECM 630 (Harvard Apparatus, at 1,100 V, 25 Ω, and 25 μF. Stable lines expressing the tagged constructs were selected selected in media with 1 μM pyrimethamine or 25 μg/ml mycophenolic acid and 50 μg/ml xanthine and cloned by limiting dilution.

RH-ΔKu80 parasites were also transiently transfected with pLIC-TgAGPAT-3HA-DHFR. pTOXO_Cas9-CRISPR::gTgAGPAT-KO was transfected in RH-ΔKu80 parasites for a simple mutant ΔTgAGPAT and in ΔTgATS2 parasites to obtain a double mutant ΔTgATS2/ΔTgAGPAT. The plasmid pMORN1-CherryRFP-MORN1/SagCAT were transfected in both RH-ΔKu80 and ΔTgATS2 parasite lines.

All other transfections were performed with 50 μg of DNA and electroporation conditions were as described above. Transfected parasites were incubated at different concentration with HFF cell 48 h prior to immunofluorescence assay.

T. gondii growth assays

- Plaque Assay

HFF monolayers were infected with 500 parasites and allowed to develop for 10 days before staining with Crystal Violet (Sigma) and cell growth assessment by light microscopy for the presence of intact HFF. To obtain statistical assessment, each strain was grown in each condition in triplicate and the plaque area in the same square unit (n = 6) are measured. Boxplot with whiskers from minimum to maximum with median.

- Cell-based assay

T. gondii growth was determined with an automatic microscope-based screening (Olympus ScanR, Japan). HFFs were seeded at a density of 10,000 cells per well into 96-well plates and were allowed to grow and equilibrate for 48 h at 37°C. Cells were then infected with 4 × 104 parasites/well. Invasion was synchronized by briefly centrifugation of plate at 250 g and placed at 37°C for 2 h. The assay was run for 30 h. Hoechst 33342 (Life technologies) stain was then loaded on live cells/parasites at 5 μg/ml for 20 min. Infected cells were fixed with PFA (3.7%) for 10 min at 37°C. A mouse anti-GRA1/Alexa488 labeling (dilution 1:500) was used to identify parasitophorous vacuoles. A total of 20 fields per well were taken using the 20X objective. Images were collected for the distinct fluorescence channels (Hoechst 33342: e.g., 360-370 nm, em. 420-460 nm and Alexa488: ex. 460-495, em. 510-550 nm). Images were then analyzed using the ScanR analysis software (Olympus, Tokyo, Japan). For Alexa488 channels images (vacuoles) an intensity algorithm module was used where a fixe threshold was defined with a minimum of 100 pixels size in order to segment the smallest vacuoles (one or two parasite). For Hoechst channel images (parasites nuclei), image process consists to apply a strong background correction and detected parasites with an edge algorithm. A minimum object size of 5 pixels and a maximum object 20 pixels larger one was chosen to discriminate each parasite. ScanR analysis module interface as in flow cytometry allow us to extract and display data as scatterplots and histograms. Using a "gating" procedure we were able to hierarchically filter selected data points with precise boundaries (e.g., number of vacuoles versus number of parasite/vacuoles). The proliferative index was evaluated by parasite/vacuole number ratio. To assess statistically, the samples were prepared in quadruplicate (n = 4).

T. gondii egress assay

WT or Δ*T*gATS2 parasites were incubated on HFF cells for approximately 26 h before aspirating medium and replacing with DMEM containing 2 μM A23187 or DMSO in quadruplicate (n = 4). Parasites were incubated for 3 min before addition of an equivalent volume of 2x fixative containing 5% Paraformaldehyde, 0.05% glutaraldehyde in PBS (final concentration 2.5% Paraformaldehyde, 0.025% glutaraldehyde). Cells were fixed for 15 min before permeabilizing with 0.025% Triton X-100 in PBS for 10 min and then Blocking overnight in blocking solution (2% FBS in PBS). Samples were then probed by immunofluorescence assay and counted manually for egress.

T. gondii Red/Green parasite invasion assay

Experiment was performed as per (Katris et al., 2014). Parasites were grown for 2 days in quadruplicate (n = 4). and harvested intracellular after replacing medium with ENDO buffer (44.7 mM K2SO4, 10 mM MgSO4, 106 mM sucrose, 5 mM glucose, 20 mM Tris-H2SO4, 3.5 mg/ml BSA, pH 8.2). Cells were scraped, needle passed, filtered and centrifuged at 1800 rpm for 10 min. Cells were resuspended to a concentration of 2.5 × 107 cells ml-1 in ENDO buffer and settled for 20 min onto host cells. Once settled, medium was aspirated and replaced with Invasion buffer (DMEM, 3% FBS and 10 mM HEPES). Parasites were allowed to invade for 15 min before fixation with 2.5% Paraformaldehyde and 0.02% glutaraldehyde. Samples were then blocked in 2% FBS in PBS overnight at 4oC. Samples were probed with mouse anti-SAG1, before washing with PBS, then permeabilized with 0.25% Triton

X-100 in PBS. Cells were then probed with rabbit anti-GAP45 and washed in PBS. Samples were then probed with Alexafluor anti-mouse 546 and anti-rabbit 488 before mounting onto slides. Cells were imaged by microscopy and invasion rate determined using ImageJ.

Plasmodium falciparum growth assays

P. falciparum NF54 wild-type parasites and FabI-KO (Vaughan et al., 2009) were maintained as previously described (Trager and Jensen, 1976) at 2% hematocrit in RPMI-HEPES supplemented with AlbuMAX II (GIBCO). Intra-erythrocytic growth assays in standard media were performed by monitoring the replication of tightly synchronous parasites (5% sorbitol) over four asexual cycles as previously described (Mi-Ichi et al., 2006; Mitamura et al., 2000). Media was replaced daily, sub-culturing were performed every 48 h when required, and parasitemia monitored by Giemsa stained blood smears. Growth assays in lipid-depleted media were performed by synchronizing parasites, before transferring trophozoites to lipid-depleted media as previously reported (Botté et al., 2013; Shears et al., 2017). Briefly, lipid-rich AlbuMAX II was replaced by complementing culture media with an equivalent amount of fatty acid free bovine serum albumin (Sigma), 30 μM palmitic acid (C16:0; Sigma) and 45 μM oleic acid (C18:1; Sigma). All assays were performed in triplicates on different days.

Immunofluorescence assay and Microscopy

Parasites were infected to HFF cells grown on coverslips as previously mentioned (Amiar et al., 2016). Primary antibodies used: Mouse anti-HA antibody (Roche, 1:1000), anti CPN60 (1:1000), anti GAP45 (1:1000), rabbit anti-ACP (1:2000), rabbit anti-TOM40 (1:3000), polyclonal rabbit anti-IMC1, anti-MIC4 antibodies (1:1000), rabbit anti-Sumo21 at (1:500) and mouse anti-Sag1 (1:500), anti-LBPA (1:500) or anti-LC3 (1:500). Secondary antibodies: anti-mouse Alexa 488 or 546, anti-rabbit Alexa 546- (ThermoFisher Scientific, 1:10000). Mitotracker (1mM) was diluted in DMEM 1:5000 (100-300 nM working concentration).

For the immunofluorescence assay (IFA) parasites were grown on confluent HFF on coverslips and fixed in PBS containing 2.5% paraformaldehyde (PFA) for 15 min at room temperature (RT). Samples were permeabilized with 0.25% Triton X-100 in PBS for 10 min at RT prior to blocking in PBS containing 3% BSA and subsequent incubation with primary antibodies then secondary antibodies diluted in the blocking solution. Labeled parasites were stained with Hoechst (1:10000, ThermoFisher Scientific) for 20 min and then washed three times in PBS before final mounting of the coverslips on a glass slide using Fluoro-Gel (Electron Microscopy Sciences). The fluorescence was visualized using fluorescence microscope (Axio Imager 2_apotome; ZEISS) with 63x objective.

Nile red staining of lipid droplets

The parasites were allowed to infect and growth in confluent monolayer HFF grown on coverslips, in the ± ATc conditions for x days and then fixed in PBS containing 2.5% paraformaldehyde (PFA) for 15 min at room temperature (RT). Samples were permeabilized with 0.25% Triton X-100 in PBS for 10 min at RT and stained with primary rat anti-HA antibody followed by detection with secondary AlexaFluor 488- conjugated goat anti-rat antibody. Thereafter, the sample coverslips were incubated for 1 h with Nile red in 1X. Lastly, three washing steps with 1X PBS were performed before proceeding to DNA staining with Hoechst. The coverslips were mounted onto a glass slide in fluorogel vefore proceeding to imaging using fluorescence microscope (Axio Imager 2_apotome; ZEISS). For visualizing nile red stained droplets yellow-gold fluorescence (excitation, 450-500 nm; emission, greater than 528 nm) was used on the axio imager. Quantification in ± ATc condition was done by counting the no. of lipid droplets per parasite.

Activity analysis in LPAAT-deficient *E. coli* strains

Escherichia coli strain deficient in LPAAT/AGPAT activity [SM2-1 ΔplsC, Coli Genetic Stock Center #7587, Yale University] (Coleman, 1990) was used to confirm LPAAT activity in both TgATS2 and TgAGPAT.

Coding sequence of *Tg*ATS2 was synthesized (Genscript). TgAGPAT coding sequence was amplified by RT-PCR using primer sets 5′-ATGGCGTCCACGCCGCTGC-3′/5′-TTAGAGACCGTGGCCTCGGTG-3′ and TgAGPATΔN-ter1-72 coding was amplified by RT-PCR using primer sets 5′-CTCAACCGCCCGCCCAGGAATTA-3′/5′-TTAGAGACCGTGGCCTCGGTG-3′. These sequences were digested and ligated into HindIII restriction site on pQE30Xa vector (Quiagen) to generate expression vectors. Additionally, gene coding for *E. coli* LPAAT activity plsC, was amplified from *E. coli* DH5alpha genomic DNA using primer sets 5′-CTATATATCTTTCGTCTTAT TATTAC-3′/ 5′-AACTTTTCCGGCGGCTTC-3′ and ligated into pQE30Xa vector. Then these acyltransferase vectors and empty pQE30Xa vector as negative control were transfected to electrocompetent cells of SM2-1 ΔplsC deficient E.coli. pREP4 repressor vector to regulate Lac promotor activity. Transformed bacterial populations were grown at 37°C in order to promote growth of all isolates. Two independent clones of each bacterial strain that harbors each plasmid-of-interest were isolated for this study. Rescue of LPAAT activity in SM2-1ΔplsC mutant was measured by the ability to grow at elevated temperature, 42°C, non-permissive temperature in LB medium as previously described (Coleman, 1990). Bacteria were first grown in LB media at 37°C to stationary phase, then the cultures were diluted to OD600 = 0.04 and finally inoculated with several dilutions (at 10-1 to 10-6) on LB plates and incubated for 24 h at permissive (30°C) and non-permissive (42°C) temperatures. All experiments were conducted in triplicate with both independent clones.

Transmission electron microscopy

Parasites were grown for 24 h in Labteks (Nunc, Thermofisher) before fixation in 0.1 M cacodylate buffer with 2.5% glutaraldehyde for 2 h. Samples were then kept in fixative. at 4oC until further processing. Sample were then post-fixed 1h with 1% osmium tetroxide in cacodylate buffer followed by overnight in 2% uranyl acetate in distilled water. After dehydration in graded series of acetonitrile, samples were progressively impregnated in Epon812, the wells were then filled with fresh resin and allowed to polymerize 48 h at 60°C. Ultrathin 70 nm section were obtained with a Leica UCT Ultramicrotome and collected on copper grids. Grids were post-stained with uranyl acetate and lead citrate before their observation on a Jeol1200EXII Transmission Electron Microscope. All chemicals were from Electron Micrsoscopy Sciences.

Lipidomic analysis by GCMS extraction from T. gondii tachyzoites

Lipid extraction and analysis of tachyzoites was performed as previously described (Ramakrishnan et al., 2012; Amiar et al., 2016; Dubois et al., 2018). Freshly egressed tachyzoites (1 × 10^8 cell equivalents) grown in standard culture (n = 4) or in starvation culture (n = 3), were metabolically quenched by rapid chilling of the cell suspension in a dry ice/ethanol bath and lipids were extracted in chloroform/methanol/water (2:1:0.8, v/v/v containing 25 nmol tridecanoic acid C13:0 as extraction internal standard) for total lipid analysis.

- For lipid quantification

Total lipid extraction was performed as described previously (Amiar et al., 2016). Parasites were prepared as described above except for the addition of 0.1 M HCl to promote PA and LPA extraction. Pooled organic phase was subjected to biphasic separation by adding 0.1 M HCl. In both protocols, the organic phase was dried with speed vaccum and dissolved in 1-butanol.

- Total lipids analysis

An aliquot of the lipid extract was dried in vacuum concentrator with 1 nmol pentadecanoic acid C15:0 as internal standard. Then the dried lipid was dissolved in the chloroform/methanol, (2:1, v/v) and derivatised with MethPrep II (Alltech). The resulting fatty acid methyl esters was analyzed by GC-MS as described previously (Amiar et al., 2016). Fatty acid methyl esters were identified by their mass spectrum and retention time compared to authentic standards. Lipid data was analyzed using Agilent® Masshunter software.

- Lipid quantification

Total lipid fraction was separated by 2D-HPTLC (Merck) with 5 μg PA(C17:0/C17:0) and 5 μg LPA(C17:0) (Avanti Polar lipids) using chloroform/methanol/28% NH4OH, 60:35:8 (v/v) as the 1st dimension solvent system and chloroform/acetone/methanol/acetic acid/water, 50:20:10:13:5 (v/v/v/v/v) as the 2nd dimension solvent system (Amiar et al., 2016). For DAG analysis, total lipid fraction was separated by 1D-HPTLC using hexane/diethlether/formic acid, 80:20:2 (v/v/v) as solvent system. The spot on the HPTLC corresponding to each lipid was scrapped off and lipids were directly derivatised with 0.5 M methanoic HCl in the presence of 1 nmol pentadecanoic acid (C15:0) as internal standard. The resulting fatty acid methyl esters were extracted with hexane and analyzed by GC-MS (Amiar et al., 2016). Resulted FAME and cholesterol-TMS was analyzed by GC-MS (5977A-7890B, Agilent). FAME was then quantified using Mass Hunter Quantification software (Agilent). All statistical analyses were conducted using GraphPad Prism software. P values of $\leq$ 0.05 from statistical analyses (Ttests) were considered statistically significant.

Stable isotope labeling of T. gondii

Stable isotope labeling using U-^{13}C-glucose (Cambridge Isotope Laboratories, USA), lipid extraction, and GC-MS analysis was performed as previously described in Ramakrishnan et al. (2012) and Amiar et al. (2016). Freshly infected HFF were incubated in glucose-free medium supplemented with 8 mM U-^{13}C-glucose. For FBS starvation study, 5% FBS was add to U-^{13}C-glucose medium in standard culture conditions and 1% FBS was add to U-^{13}C-glucose medium in starvation culture condition. Parasites were harvested 72 h post-infection and metabolites extracted as above.

Phospholipid import assay

Freshly lysed cultures of WT or ΔTgATS2 parasites (n = 3) were harvested, filtered and resuspended in DMEM to a concentration of approximately 2 × 108 cells ml-1. Cells were then mixed with a 2x solution containing 10 μg ml-1 NBD-PA or NBD-PC (5 μg/mL final) and incubated at 37oC. Parasites were then spun down, resuspended in PBS. PFA was then added to a final concentration of 2.5%, and cells were fixed for 15 min before being spun down again and resuspended in 1xPBS. Parasites were smeared onto polyethyleneimine coated coverslips, and then probed with anti-SAG1 primary (1:1000) and anti-mouse Alexa 546 secondary antibodies (1:10000) by immunofluorescence microscopy, stained with DAPI (1:10000) and mounted onto slides. Samples were imaged by microscopy. SAG1 labeling was used to identify parasites using ImageJ and then estimate the amount of NBD-lipid uptaken by the parasites.

QUANTIFICATION AND STATISTICAL ANALYSIS

Statistical analyses for all experiments were performed with Prism software v7 (GraphPad). In experiments comparing only two groups, t test with Holm-Sidak correction were used to compare the experimental group with the control group. For other experiments including 3 groups, non-parametric ANOVA tests (Sidak correction for multiple tests) were used. Individual p values are indicated in each figure. Each experiment was done in n = 3 otherwise mentioned in material metthods. For lipidomic analysis,

Agilent® Masshunter software, was used for fatty acid analysis and subjected to statistical analysis as described above. All error bars present standard error of mean, otherwise mentioned individually.

DATA AND CODE AVAILABILITY

No unique code or software was generated in this study. All datasets generated and analyzed during this study are available upon request to the lead contact Cyrille Botte (cyrille.botte@univ-grenoble-alpes.fr).